

Imperial College London

MENG INDIVIDUAL RESEARCH PROJECT

IMPERIAL COLLEGE LONDON

DEPARTMENT OF CIVIL AND ENVIRONMENTAL ENGINEERING

Simulating the Effect of Droplet Size on COVID-19 Particle Dispersion

Author:

Hamish A. Thomas

Supervisor:

Dr. Maarten van Reeuwijk

Word Count:

11,985

Publication Date: 4th June 2021



Simulating the effect of droplet size on COVID-19 particle dispersion.

Hamish A. Thomas¹

Supervisor: Dr. Maarten van Reeuwijk¹

*Imperial College London, Department of Civil and Environmental Engineering,
Skempton Building, South Kensington Campus, London, SW7 2AZ*

June 4, 2021

Abstract: In this research project, the effects of droplet size on COVID-19 particle dispersion will be simulated and analysed in two different scenarios - a standard quiescent background and a decaying turbulent background. The simulations will be conducted using a DNS code which essentially solves incompressible fluid flows within cubic domains. The DNS data will be used to produce statistics that can be analysed in detail for the two cases. The results from this report will predominantly be analysed using the concept of the Stokes number and the physics that underpins this relation. In the quiescent scenario, the results are dictated by the particle response time, as the local fluid flow scales will be fairly constant throughout the domain. The results in the quiescent case are well established, and the radius/diameter will be the main factor influencing the particle behaviour. However, in a turbulent scenario, the increased range of flow (length) scales induced by the heightened vorticity in the background will lead to different Stokes numbers for particles of the same radius. This will ultimately cause far greater variation in particle behaviour, showing that, whilst particle size is an important factor in COVID-19 dispersion, the background environment is also a vital part of the picture.

Keywords: SARS-CoV-2, COVID-19 dispersion, Direct-Numerical Simulation, Respiratory Droplets, Aerosols, Computational Fluid Dynamics.

1 Introduction

COVID-19, a disease caused by 'severe acute respiratory syndrome coronavirus 2' (SARS-CoV-2), was first discovered in 2019 in Wuhan, China, and has led to the ongoing global pandemic which has caused widespread societal and economic disruption (WHO 2021). As a respiratory disease, COVID-19 affects human airways, with symptoms ranging from breathing difficulties and mild pneumonia, to respiratory failure in very severe cases. The virus that causes COVID-19 is considered to be highly pathogenic, and is transmitted via several key pathways (V'kovski et al. 2021). All current evidence suggests that COVID-19 is highly contagious and very transmissible, with the ability to spread quickly through a given community or population, and this has generated a research focus into the means by which the virus can be transmitted.

1.1 Motivation

The ongoing COVID-19 pandemic has been the defining issue of the past year, making the dispersal and transmission of respiratory diseases a hugely topical area of research. At the time

of writing, the World Health Organisation states that there have been over 171 million confirmed cases of COVID-19, with over 3.5 million deaths (WHO 2021). Based on this data, approximately 2.2 % of the global population has had a positive diagnosis of COVID-19, and this value is expected to rise until the global vaccination 'roll out' has produced sufficient international immunity. Current research has led to a better understanding of the airborne dispersion and transmission of COVID-19 particles. In particular, numerical approaches (similar to that used in this project) along with experimental methods (such as background oriented schlieren and laser diffraction approaches) have provided great insight (Viola et al. 2021). However, due to the large range of particle sizes that are emitted by the carriers of respiratory diseases, further investigation into the local dispersion of different sized COVID-19 particles may be particularly useful. This research might also help to confirm the findings within other areas of this field (both numerical and experimental) and ultimately, offer greater clarity regarding the virus transmission process.

1.2 COVID-19 transmission routes

SARS-CoV-2 laden particles are projected from an infected person's nose or mouth as they cough, breathe, talk or sneeze, and can find their way to an uninfected host via several key transmission routes. Importantly, transmission will occur if these particles make passage through the airways or eyes of an uninfected individual and eventually come into contact with epithelial cells within the body (Moriyama et al. 2020).

Firstly, COVID-19 can be passed on via airborne transmission, which occurs when the aforementioned virus laden particles make a direct passage between two individuals, without coming into contact with other environmental bodies. Some research literature classifies airborne transmission as that which occurs at large distances/ranges via aerosol particles alone (Tang et al. 2021a). However, this investigation will incorporate transmission from both aerosol particles and droplets into the definition of 'airborne transmission', as both particle types are transmitted via projection through the atmosphere. The difference between these two particle types will be discussed extensively in section 1.3. Importantly, for airborne transmission, the probability of infection will depend on the number of particles inhaled and the 'characteristic dose' of infection, which is a parameter that varies for different respiratory viruses and different surrounding environments (Stone 2021).

It is also believed that COVID-19 can be spread via contaminated surfaces (also known as fomites) that become populated with virus laden droplets/particles that have been exhaled by an infected individual (Galbadage et al. 2020). It is widely accepted that uninfected individuals can make physical contact with these fomites, and bring the virus into contact with their eyes and airways through their own means. Environmental factors will play a large role in the transmission of respiratory viruses via any route, but they will be particularly relevant when analysing the stability of particles found on fomites (Galbadage et al. 2020). The different transmission paths are highlighted below in *Figure 1*. Although, the fomite transmission pathway is considered to be important, this research project will only analyse the airborne transmission of COVID-19.

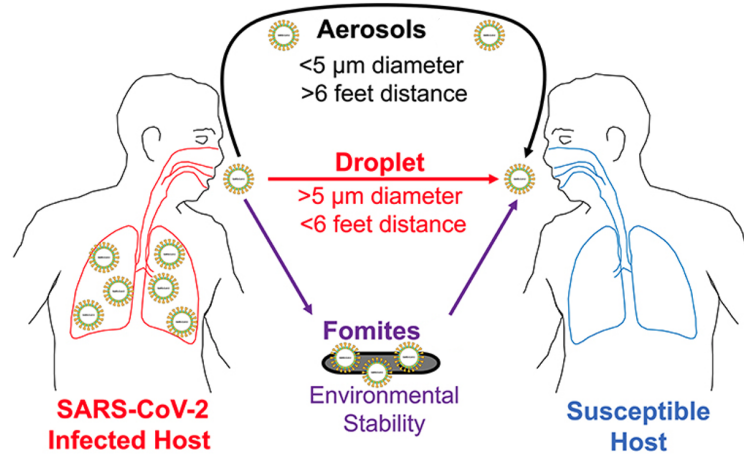


Figure 1: Graphic showing the different transmission paths for COVID-19 (Galbadage et al. 2020)

1.3 Droplets and Aerosols

The virus that causes COVID-19 can be transmitted through the air by small particles, which, depending on their size (diameter) can often be classified as either *droplets* or *aerosols*. It is well documented that the properties of these droplets/aerosol particles, such as their size, shape and evaporation kinetics, will significantly affect the characteristics of their transport within a system (Abuhegazy et al. 2020).

However, there is an important distinction to be made between 'aerosols' and 'droplets', especially as the difference between the two is still somewhat debated. Based on updated information from the World Health Organization (WHO), it is generally recognised that 'droplets' are small accumulations of sputum (mucus and saliva) that are directly sprayed from the mouth/nose during coughing/sneezing/exhalation (Debczak 2020). Importantly, these respiratory droplets can vary in size from what is perceived as 'visible' all the way down to 'invisible' particles that range in size between 5 and 10 μm . Importantly, almost all droplet particles that are passed from an infected person are likely to be laden with the virus (Debczak 2020). It is very important to note that saliva and mucus particles (also known as sputum particles) are heavier than air, and are thus pulled downward by gravity, leading to gravitational sedimentation. In general, the larger the particle's diameter, the greater its weight and the quicker it will fall and be deposited on the ground or on a nearby surface.

On the other hand, Aerosols are purely invisible particles that are emitted as minute respiratory droplets or, alternatively form when larger respiratory droplets evaporate before they can be deposited on the ground or a nearby surface. The droplets or, in the case of evaporation, droplet nuclei, that are classified as aerosols tend to be less than 5 μm in diameter. This arbitrary size cut-off at 5 μm is the most important distinction between respiratory droplets and aerosols and even though it is not a 'defined threshold', it will at times be used in this report (Zuo et al. 2020). However, some research indicates that many people are taking this cut-off size too literally, and in fact, aerosol scientists believe that any particle suspended in the air (that can be inhaled) should be classified as an aerosol (Tang et al. 2021b). In some cases, aerosols are even defined by their lifespan in the air, or the range at which they can be transmitted or

detected. For example, it is believed that respiratory droplets (greater than $5\text{ }\mu\text{m}$) generally have a limited transmission distance of $< 2\text{m}$, whilst studies of aerosols show they can be detected at much greater distances and, unlike droplets, can still be present in the atmosphere after 2-3 hours (Zuo et al. 2020). Some of the key misconceptions surrounding aerosols and droplets are highlighted in *Table 1*, which shows the difference between the clinical and scientific perception of the droplets vs. aerosols debate (Tang et al. 2021a).

Table 1: Difference between clinicians, aerosol scientists and the general public in understanding the key terminology of airborne transmission.

Term	Clinicians	Aerosol Scientists
Aerosols	Particles $< 5\text{ }\mu\text{m}$ in diameter that mediate airborne transmission; produced during aerosol-generating procedures.	Collection of solid or liquid particles suspended in a gas (e.g. air).
Droplets	Particles $> 5\text{ }\mu\text{m}$ in diameter that fall rapidly to the ground within a distance of 1-2m from their source.	Liquid particles

Ultimately, it is not appropriate for aerosols and droplets to be compared and defined by the distance that they travel or the period of time they remain suspended in air (Tang et al. 2021b). Virus-laden particles of all sizes will be emitted in a 'plume of exhaled breath' and although 'aerosols' can remain airborne for long periods and be carried long distances ($>2\text{m}$), the concentration of these particles will also be very high at conventional, short distances. It is also possible that small droplets ($5\text{ }\mu\text{m} < \text{diameter} < 10\text{ }\mu\text{m}$) can be carried further than 2m and remain present in the air for a very long period of time. Distinguishing between these particle categories based on their projected range and lifespan is an outdated approach, given the continuum of particle sizes that are emitted in a typical respiratory release (Tang et al. 2021b). This research project will use the arbitrary size distinction (of $5\text{ }\mu\text{m}$) when discussing the behaviour of aerosols and droplets, but it will also aim to ultimately prove that these arbitrary cut-offs between the particle types (which are based on size, lifespan, distance travelled, etc.) are ineffective. This is because, in reality, the behaviour of a particle (lifespan and distance travelled) will depend greatly on a variety of different factors, which can be encompassed in the particle's Stokes number (see Section 2.2). Based on this, the particle behaviour will depend not only on its size, but also on the surrounding environment and the dynamics of the flow within which the particle is transported. This can induce hugely varied particle behaviour, that can violate the arbitrary droplet-aerosol definitions based around size, range (distance travelled) and lifespan. The research in this report will aim to show this.

1.4 Objectives

The **primary objective** of this research project is to investigate the effects of different particle sizes on the dispersion of COVID-19 particles. This will be done using direct numerical simulation (DNS) in which the COVID-19 particles will be modelled as point spheres. It will

be carried out on a high-processing computer by numerical code. This numerical code can be tuned (by altering initial parameters and conditions) to effectively replicate a human cough. The investigation will focus primarily on how aerosol/droplet dispersion occurs on a small, localised scale by modelling the interaction between the particle behaviour and flow dynamics. Notably, an Eulerian approach will be applied to the (air) flow field, whilst a Lagrangian approach will be adopted for the individual COVID particles. An appropriately selected range of particle sizes will be seeded into a cough simulation and, by processing the results obtained, conclusions will be made regarding the effects of different particle sizes. The effects of particle size will be quantified by post-processing the DNS data, obtaining values for different indicators such as particle spread, average centre of mass, settling time and settling velocity, which can ultimately be compared for different size ranges.

Importantly, these effects will be examined in two different background scenarios. Firstly, the particle dispersion associated with a cough into a quiescent background will be analysed - this will be regarded as the 'base scenario'. Once this has been completed, the numerical code will be used to create a simulation for background grid turbulence, into which a cough with the same initial conditions will be projected. The DNS approach adopted will be particularly effective at capturing these small-scale turbulent dynamics, as it can resolve down to the smallest scales in a multi-scale turbulent flow (the Kolmogorov scale) (Nair 2021). This will allow for the evaluation of a **secondary project objective**, examining what the presence of background turbulence will do to the speed, distribution and spread of the exhaled COVID particles. Finally, by showing how turbulence can induce great variation in particle behaviour for a range of different particle sizes, this research will demonstrate the limitations of arbitrarily distinguishing between droplets and aerosols based upon size, range or lifespan. It will show that droplets and aerosols should be viewed as a continuous spectrum of respiratory particles, whose behaviour is not defined arbitrarily by a size/range/lifespan cut-off, but by the particle Stokes Number which depends on both the particle characteristics **and** the background conditions.

2 Background

2.1 COVID-19 Particle Physics

Ultimately, COVID particles (both aerosols and droplets) within a cough-induced velocity field can be modelled as 'small rigid inertial point spheres within a non-uniform flow' (Nair 2021). A free body diagram of the point sphere (particle) is shown below in *Figure 2* and this highlights some of the key force components that act upon it. This diagram (and the model used in this report), assume that the particle is coughed initially in the positive x-direction, with no transverse or vertical *initial* velocity components. The force components outlined in *Figure 2* are as follows: F_b is the buoyancy force, W is the weight, F_d is the drag force and \underline{u} is the initial horizontal velocity component that gives rise to an inertial/flow force in the x-direction.

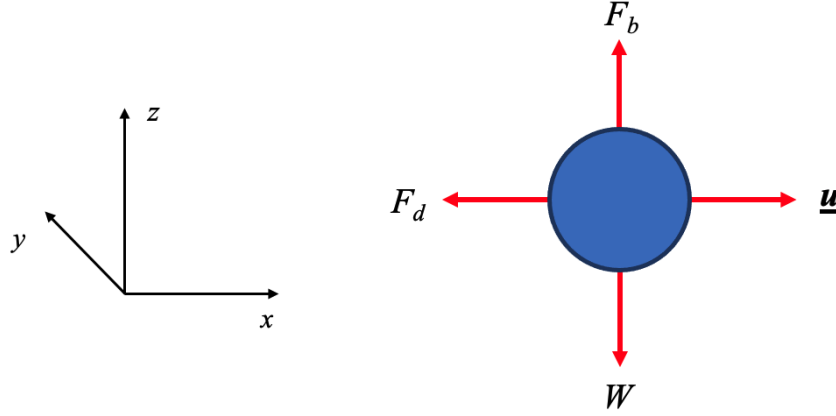


Figure 2: Simple free body diagram depicting the key forces that act on a COVID-19 particle.

Importantly, different combinations of the forces depicted in *Figure 2* will act on different particles (depending on their properties). For example, due to their size, large droplets will be subject to greater gravitational settling forces (weight) than smaller particles, but will also experience larger drag components, due to their greater radii (Abuhegazy et al. 2020). The free-body diagram does not highlight other forces such as 'added mass' and 'Basset force' that arise in response to the motion of the sphere, but these will be included in the governing equations given below.

The forces that control the physical behaviour of these particles (within a Lagrangian Framework) are summarised by the following governing equations, which are taken from the work of Maxey & Riley (1983), who reformulated the equations of motion for small rigid spheres in a non-uniform flow. This governing equation is derived from Newton's II Law and equates the rate of change of momentum of the particle (LHS of the equation), with the resultant force that acts on the particle (RHS of equation).

$$m_p \frac{d\mathbf{v}}{dt} = \underbrace{(m_p - m_f)g}_1 + \underbrace{m_f \frac{D\mathbf{u}}{Dt} \Big|_{\mathbf{X}(t)}}_2 + \underbrace{-\frac{1}{2}m_f \left(\frac{d\mathbf{v}(t)}{dt} - \frac{d}{dt} \left(\mathbf{u}(\mathbf{X}, t) + \frac{1}{10} R^2 \nabla^2 \mathbf{u} |_{\mathbf{X}(t)} \right) \right)}_3 \quad (1)$$

$$\underbrace{-6\pi\mu R \mathbf{V}(t)}_4 - \underbrace{6\pi\mu R^2 \int_0^t \frac{d\mathbf{V}(\tau)}{d\tau} \frac{d\tau}{(\pi\nu(t-\tau))^{\frac{1}{2}}}}_5$$

Where:

$$\mathbf{V}(t) = \mathbf{v}(t) - \mathbf{u}(\mathbf{X}(t), t) - \frac{1}{6} a^2 \nabla^2 \mathbf{u} |_{\mathbf{X}(t)} \quad (2)$$

Here, $\mathbf{X}(t)$ and $\mathbf{v}(t)$ are the particle position and velocity vectors at time t , m_p is the mass of the sphere, R is the radius of the sphere, m_f is the mass of fluid displaced by the sphere, $\mathbf{u} = (u, v, w)$ is the fluid velocity vector in the x , y and z directions respectively, μ is the dynamic viscosity of the fluid and finally, $\mathbf{g} = -g\vec{e}_z$, where $g = |\mathbf{g}|$ is the acceleration due to gravity and \vec{e}_z is a unit vector in the direction of the positive vertical axis (z). Additionally,

d/dt is the time derivative in a reference frame moving with the particle and D/Dt is the time derivative following the fluid element (Nair 2021). The terms containing $a^2 \nabla^2 \mathbf{u}$ are referred to as the Faxén correction terms and these account for the non-uniformity of the flow at scales comparable to the particle diameter (Nair 2021). The terms grouped on the right hand side of the above equation correspond to the forces acting on the spherical particle and are as follows:

1. The buoyancy force
2. The force on the particle exerted by the flow field
3. The added mass (force required to accelerate the mass of fluid surrounding the sphere)
4. The viscous drag force (Stokes Drag)
5. The Basset history force (due to the development of a lagging boundary layer)

In their current form, the force components in the equation of motion given above require great computational expense to evaluate. Therefore, simplifications will be made to the equation of motion above so that only the 'dominant forces' are considered in the DNS code, reducing the need for significantly large computational effort (Nair 2021). The Faxén correction terms are neglected and, because the density of the particles is much greater than that of the surrounding fluid, the added mass and pressure force will be negligible when compared to the Stokes Drag. Finally, although the Basset history force does impact the motion of particles, it is of a smaller order of magnitude than the Stokes drag, and its calculation requires the full history of particle acceleration (Nair 2021). It will therefore also be neglected, primarily as a means of reducing computational expense. Based on these simplifications, equation (1) can be rewritten as follows:

$$m_p \frac{d\mathbf{v}}{dt} = 6\pi a \mu (\mathbf{u}(\mathbf{X}, t) - \mathbf{v}(t)) + m_p \mathbf{g}. \quad (3)$$

Equation (3) now represents a simplified version of Newton's II Law (applied to a point sphere), where the rate of change of momentum is equal to the force balance between the viscous drag force (produced by the motion of the sphere relative to the surrounding fluid) and the weight (Nair 2021). Dividing equation (3) by the mass of the sphere and adding equation (5), which governs the particle movement, gives the final simplified set of governing equations that will be used in the DNS code to control particle behaviour:

$$\frac{d\mathbf{v}}{dt} = \frac{9\mu}{2\rho_p R^2} (\mathbf{u}(\mathbf{X}, t) - \mathbf{v}(t)) + \mathbf{g}. \quad (4)$$

$$\frac{d\mathbf{X}}{dt} = \mathbf{v}(\mathbf{X}, t) \quad (5)$$

It is important to note that the governing equations for particle dynamics (in a Lagrangian Framework) shown above are different to those that govern the flow - these are governed by the continuity equations and the Navier-Stokes equations (in an Eulerian Framework) ((Nair 2021). More details on this can be found in section 2.

The governing equations given above can also be used to define the settling velocity of a particle, a property that is very important to this research. Settling velocity is defined as the

terminal velocity at which a particle will settle under the effects of gravity in stationary air/fluid (Finlay 2019). In the quiescent background scenario, once the initial velocity field created by the cough reduces over time, the background 'fluid' will tend towards a stationary condition. In this case, it is expected that the horizontal inertial force component will reduce in line with the field velocity, leading to horizontal force equilibrium for the particles. Additionally, the forces in the vertical component (namely the Stokes Drag force, buoyancy and weight) will balance after a certain period of time, creating a scenario in which the particles will be in full equilibrium falling steadily towards the ground. Based on this concept, it is believed that as the amplitude of the flow and resulting velocity field reduce, the vertical components of particle velocity will tend towards the settling velocity of the particle (Finlay 2019). Analysing the trends in vertical particle velocity over time should allow for a practical interpretation of settling velocity, as well as a comparison between the experimental and theoretical results.

Assuming that a particle is in a force equilibrium, falling at a constant velocity, modifications can be made to equation (4) to derive the settling velocity of a given particle. Once the particle has equilibrated, the acceleration component tends to zero ($\frac{dv}{dt} \rightarrow 0$) and the velocity component of the drag force will be replaced with a constant settling velocity ($\mathbf{u}(\mathbf{X}, t) - \mathbf{v}(t) = v_s$). The force balance can then be rearranged to give the following settling velocity for a perfectly spherical, non-rotating particle solely under the influence of Stokes drag and weight:

$$v_s = \frac{2\rho_p g R^2}{9\mu} \quad (6)$$

Where, v_s is the particle settling velocity, ρ_p is the density of the particle, g is acceleration due to gravity, R is the radius of the sphere and μ is the dynamic viscosity of the surrounding fluid. Ultimately, the relationship given in equation (6) can be used to derive the theoretical settling velocity for different particle sizes, which can be compared with the experimental values produced by DNS.

2.2 Particle Response Time and Stokes Number

The behaviour of particles with a range of different sizes can be effectively analysed through the particle response time, the Stokes Number and the physics that underpins these concepts. The particle response time (also known as the relaxation time) is the time taken for a particle to react to change in the surrounding fluid flow and/or a new condition of forces (Liu 2020). Importantly, different characteristic particle sizes will have different particle response times, as this property depends on the mass and mechanical mobility of the particle (Liu 2020). Within the Stokes regime, the application of Newton's II Law can be used to derive an analytical relationship for the particle response time (τ_p) (Lloyd 2003). This equation is given as follows:

$$\tau_p = \frac{\rho_f D^2}{18\mu_f} \quad (7)$$

Here, ρ_f is the fluid density, D is the diameter that characterises the particle and μ_f is the dynamic viscosity of the fluid. The Stokes regime is classified when the particle Reynolds number, shown in equation (8), is less than unity ($Re \ll 1$).

$$Re = \frac{\rho_f U D}{\mu_f} \quad (8)$$

Here, U is the surrounding flow velocity. Equation (7) clearly shows that the particle response time is directly proportional to the square of the particle diameter. As a result, one would generally expect small particles to exhibit low values of τ_p , with particle velocities approaching the surrounding flow velocity very quickly. Conversely, larger particles with greater values of τ_p take a very long time to approach the velocity of the fluid flow.

It is important to note that the particle response time, although a good indicator, cannot completely describe the dynamics of moving particles within a fluid, particularly if the fluid behaviour is more erratic than it would be in a quiescent or laminar scenario. The particle response time accounts for the time taken for a particle to respond to changes in the flow - but an understanding of the timescales of the flow (and the regularity of its changes) is needed to complete this picture, this can be done with the Stokes number. The Stokes number (Stk) is the ratio of the particle response time to the characteristic time scale of the fluid flow (Nicolaou & Zaki 2015):

$$Stk = \frac{\tau_p}{\tau_f} \quad (9)$$

Here, the numerator represents the time particles take to react to changes in the fluid flow, whereas the denominator represents the time scale over which changes in the fluid flow actually arise. Therefore, if a particle has a Stokes number much lower than 1, then the particle response time is much lower than the fluid time scale ($\tau_p \ll \tau_f$) and the particle reacts immediately to changes in the fluid flow. On the other hand, if a particle's Stokes number is much larger than 1, then the particle response time is much larger than the fluid time scale ($\tau_p \gg \tau_f$) and in this case the particle is unaffected by the change in fluid flow. This concept will become very important when analysing the turbulent case, as the background grid turbulence will induce a much greater range of time scales for the fluid flow and, unlike the 'base case' scenario, this will mean that particles with similar radii are more likely to have different Stokes numbers and therefore behave in different ways. The time scales in a turbulent environment will generally be much smaller and more varied than those in a quiescent environment, spreading down to the smallest possible time scale found in a turbulent flow called the Kolmogorov scale (Nair 2021). Because turbulent backgrounds are characterised by smaller time scales τ_f , if two particles with the same radii and particle response time τ_p are placed in environments with different turbulence intensities, the particle in the more turbulent environment will have a higher Stokes number, and is therefore more likely to be unaffected by the surrounding fluid flow.

2.3 Background Turbulence

Turbulence is fluid motion that is characterised by the presence of chaotic eddies, which have been disturbed from a previously calm state by forces (induced by pressure or flow). Once this report's simulations have been conducted in a quiescent background, the DNS code will be used to produce a background condition characterised by *homogeneous isotropic grid turbulence*, into which the model cough will be projected. Grid turbulence is turbulence that is

typically generated by fluid moving through a grid or screen, often found in a wind tunnel or water channel. The grid causes the fluid flow to break up, leading to the formation of many different eddies with varying scales. Grid turbulence is approximately homogeneous and is generally characterised by the value of turbulent kinetic energy, which typically decays as $1/x$, where x is the distance downstream (AMS 2012). Although homogeneous isotropic turbulence is idealised and would never be encountered in nature, its application can allow inferences to be made regarding the behaviour of particles in a turbulent background (MIT 2020). The terms *homogeneous* and *isotropic* are defined in detail (with respect to turbulence) below:

- **Isotropic** - A turbulent flow is considered isotropic if rotation and buoyancy can be neglected and there is no mean flow present. This is because rotation and buoyancy can introduce anisotropy between the vertical and horizontal directions (MIT 2020).
- **Homogeneous** - A turbulent flow is considered homogeneous if there are no spatial gradients in any averaged quantity. Essentially the statistics of the turbulent flow are not functions of space (MIT 2020).

As a result of these properties, the mean zonal velocity within this type of turbulent field will be zero. In this grid turbulence environment, the kinetic energy will be injected into the system (through the 'grid') at large scales, and will be dissipated at much smaller scales, following an energy cascade. The smallest possible scale of a turbulent flow is referred to as the 'Kolmogorov Scale', and this will be an important factor when evaluating the changes to the Stokes number brought about by background turbulence (MIT 2020). The Kolmogorov length scale (η) and velocity scale (μ_η) are given below (MIT 2020).

$$\eta = \left(\frac{v^3}{\varepsilon} \right)^{1/4} \quad (10)$$

$$\mu_\eta = (v\varepsilon)^{1/4} \quad (11)$$

where v is the kinematic viscosity of the fluid surrounding the particle and ε is the average rate of turbulent kinetic energy dissipation per unit mass. The Kolmogorov length scale will allow for the analysis of the particle Stokes number, whilst the velocity scale will allow for the evaluation of a non-dimensional settling parameter (S_v), which is given as follows:

$$S_v = \frac{v_s}{\mu_\eta} \quad (12)$$

This non-dimensional parameter incorporates the particle settling velocity (v_s) found in equation (6) and characterises the level of interaction between turbulence and gravity (Nair 2021). The most important aspect of the background grid turbulence (in the context of this report) will be its effects on the distribution and behaviour of COVID particles. As mentioned previously, the presence of turbulence will hugely alter the flow (time) scales in comparison with the quiescent scenario, which will have large knock-on effects on the Stokes numbers of individual particles. The smaller scales will lead to higher values of the Stokes number for

individual particles, which in turn will make them less likely to respond to changes in the flow field. The impacts of turbulence are studied in the results section of this report.

2.4 Respiratory Releases

Understanding the characteristics of different respiratory releases will be vital for this project's simulations. Coughing, sneezing and talking will all produce different particle sizes and initial velocities, and this information will be highly relevant to this report's simulations, helping to ultimately decide which respiratory release should be modelled. Extensive research regarding the particle characteristics for different respiratory releases is summarised below:

- **Exhalation:** Experimental analysis of exhalation (and conversational talking) show that 99% of expired particles are $< 1\mu\text{m}$ in diameter, with 75% less than $0.5\mu\text{m}$ (Wurie et al. 2013). Another study shows that the median particle size for 'exhalation' is approximately $0.28\mu\text{m}$ (Wan et al. 2014). Interestingly, the report by Wurie et al. also indicates that there is a large variation in the particle load (e.g. particles released per unit volume of exhalation) from person to person. Regardless, based on the expected particle size shown by these studies, it is clear that small 'aerosol' particles will be of primary interest when analysing the transport mechanics associated with simple exhalation.
- **Coughing:** A different study focused explicitly on the size distribution of droplets and particles emitted/projected exclusively by coughing (Yang et al. 2007). This research found that the size distribution for most coughed droplets ranged between $0.62\mu\text{m}$ and $15.2\mu\text{m}$, with a mode of $8.35\mu\text{m}$ (although the overall distribution of droplet sizes produced by coughing is multimodal, with peaks at $1\mu\text{m}$, $2\mu\text{m}$ and $8\mu\text{m}$). Regardless, coughing clearly produces a larger range of particle sizes, some of which are categorised as droplets but some of which will alternatively be considered as aerosols. Therefore, the transport dynamics of both droplets and aerosols will be relevant in this case.
- **Sneezing:** A final study, which measured the droplet sizes associated with sneezing, has shown that droplet diameters are considerably larger for this respiratory release (Han et al. 2013). Based on the distribution of droplet diameters, it would be feasible to fit either a unimodal distribution or a bimodal distribution to the data found in this study. Analysis shows that the geometric mean of the droplet diameter for a unimodal distribution is $360.1\mu\text{m}$, however, for a bimodal distribution, the geometric mean is $74.4\mu\text{m}$. This highlights the far greater variation in droplet size associated with sneezing. Overall, the particle diameters associated with this projection method are considerably larger than those of exhaling or coughing, suggesting that for this projection method, 'aerosol' particles will be considerably less relevant. Although there may be some smaller droplets inadvertently produced by sneezing, it is clear that large droplets will account for the majority of the viral transport associated with sneezing.

The results given above are summarised in *Table 2*. Due to the fact that both the 'aerosol' and 'droplet' particle categories play a *key role* in the mechanics of a cough, the simulations conducted in this report will aim to closely replicate the initial conditions of this respiratory release. However, it is important to note that some larger particles (like those within the size

range of sneezing), will be included in this research's simulations. This is done for two key reasons. Firstly, it is highly probable that some of these large particles (up to a size of 75-100 μm) could be inadvertently produced by a cough (particularly a deep one), and thus an understanding of their behaviour is important. Secondly, simulating a large range of particle sizes (from small aerosols up to large droplets) will help to satisfy the project's main objective of comparing the effects of these different size categories.

Table 2: Summary of the dominant particle types for different respiratory projection methods.

Projection Method	Dominant Particle Type	Approximate Diameter (μm)
Exhalation	Aerosols	< 1 (Average = 0.28)
Coughing	Aerosols + Droplets	0.58-15.2
Sneezing	Droplets	> 20 (Average = 75)

2.5 Relevant Coughing Characteristics

As is mentioned in section 2.4, this report's simulations will try to replicate a human cough, as this type of respiratory release characteristically contains both aerosols (particles $< 5\mu\text{m}$) and respiratory droplets (particles $> 5\mu\text{m}$). One of the key initial conditions that needs to be replicated is the **initial velocity**. Based on a study of 29 volunteers, initial coughing velocities range between 1.5m/s and 28.8m/s, with an overall average of 10.2m/s (VanSciver et al. 2011). No correlation was found in this study for sex or weight. These results are similar to those obtained by Zhu et al. (2006) and Chao et al. (2009), who both used particle image velocimetry to deduce average coughing velocities of 11.2 m/s and 11.7 m/s respectively. Based on this research, the guidance of VanSciver et al. will be used and an initial velocity of 10 m/s will be applied to simulations. This report also states that, on average, 6.7 mg of saliva/sputum are emitted during a cough (VanSciver et al. 2011). At the pre-specified density of 1.012 g/ml, this corresponds to a total volume of 6.62 mm^3 . Importantly, this project's simulations will aim to prevent the total (initial) particle volume from deviating away from this target value.

It is also important to note that there are particle size distributions that characterise coughs. As mentioned previously, the particle size distribution produced by a cough takes the form of a bimodal distribution. However, there is contrasting research from both Yang et al. and de Oliveira et al. about where the peaks of this bimodal distribution actually lie. For this reason, a uniform distribution will be adopted for the simulations, which will divide the number of particles equally between different radius categories. This decision has also been made to allow equally weighted comparisons between different particle sizes. As mentioned previously, even though the range of particle sizes for a cough is approximately 0.58-15 μm , it is still plausible that larger droplets $> 20\mu\text{m}$ could be produced, particularly in deep coughs. Particles up to the size of around 100 μm in diameter will therefore be simulated and analysed, providing an understanding of the difference in behaviour between very large and small droplets.

3 Methodology

3.1 SPARKLE

The DNS code called SPARKLE, that solves the incompressible Navier-Stokes equations under the Boussinesq approximation, will be used to run simulations for this project (Nair 2021). This code has been written in Fortran, but is compiled to run on a high-processing computer (cx2 was used for this investigation). This DNS code operates in an Eulerian-Lagrangian framework, which will allow for the modelling of feedback between the flow field and the particle behaviour. An Eulerian framework will be applied to model the flow, whereas a Lagrangian particle tracking routine will be used to control the behaviour of the individual point spheres. Within the Eulerian component, the code that governs the flow is based on a finite volume discretisation of the following governing equations - the continuity and Navier Stokes equations (Craske & van Reeuwijk 2015):

$$\nabla \cdot \mathbf{u} = 0, \quad (13)$$

$$\frac{\partial \mathbf{u}}{\partial t} + \mathbf{u} \cdot \nabla \mathbf{u} = -\nabla P + \nu \nabla^2 \mathbf{u}, \quad (14)$$

where $\mathbf{u} = (u, v, w)$ is the velocity vector with the horizontal, transverse and vertical velocity components respectively, P is the kinematic pressure and ν is the kinematic viscosity (Nair 2021). The advection-diffusion equation is also a governing equation for SPARKLE, but has been ignored for this simulation, as no scalars are being advected. SPARKLE is based on a symmetry-preserving finite volume discretisation, in which variables are arranged in a staggered manner over the grid (Nair 2021). In particular, SPARKLE employs the symmetry-preserving method of Verstappen & Veldman (2003), which conserves mass, momentum and energy, and is also accurate to fourth order (Craske & van Reeuwijk 2015). Full details of the numerical scheme, parallelisation and boundary conditions can be found in the appendix of Craske & van Reeuwijk (2015). Within a given cell, the transported variables are defined at the centre of a control volume, while the fluxes are defined on the face centres. *Figure 3* highlights a standard single computational cell in SPARKLE, which is shown in 3-dimensions (a) and also in 2-dimensions (b). In this diagram, arrows represent the location of fluxes whereas dots represent the location of transport quantities. The velocity component u is defined at (x_b, y_c, z_c) , the component v is defined at (x_c, y_b, z_c) , the component w is defined as (x_c, y_c, z_b) and the scalars are defined at the cell centre (x_c, y_c, z_c) (Nair 2021). Here, the subscript b stands for the boundary coordinate and the subscript c stands for the centre coordinate. As mentioned previously, the governing equations will be solved numerically across the domain, and this will be done subject to specific boundary conditions. A 2-dimensional 'pencil' domain decomposition will be applied to this problem, in which there are multiple processors in both the y and z -directions, but only one processor in the x -direction. This particular decomposition, which creates very long and thin sub-domains, is commonly applied to boundary value problems and is perfectly workable for the SPARKLE code.

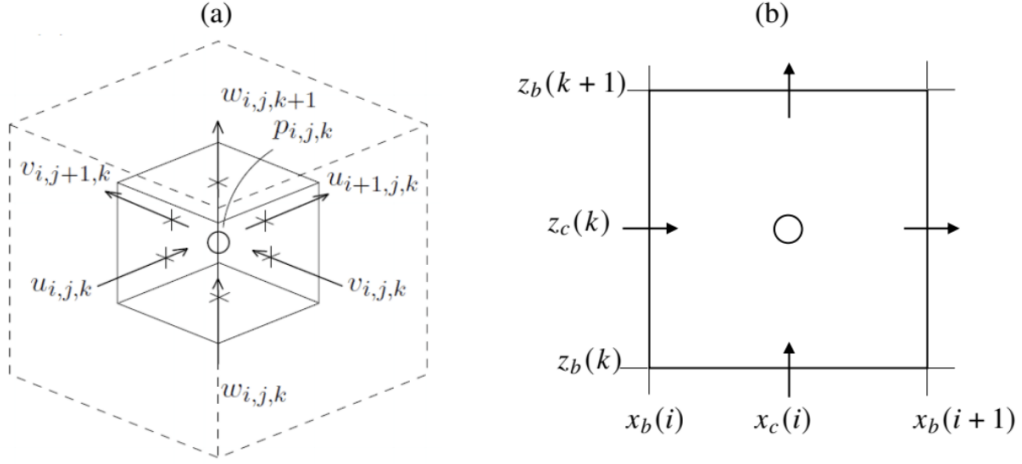


Figure 3: Diagrams representing the cells found in SPARKLE: (a) Single computational cell showing the staggered arrangement of variables. (b) A two-dimensional section of a cell centred in the grid (Nair 2021).

As mentioned previously, SPARKLE operates in a hybrid Eulerian-Lagrangian framework, and while equations (13) and (14) control the flow, SPARKLE also contains a Lagrangian particle tracking routine, which is governed by equations (4) and (5) and incorporates the particle physics discussed in section 2.1 (Nair 2021). The Lagrangian nature of the particle tracking routine means that equations (4) and (5) (which dictate the rate of change of momentum and velocity of a given point sphere) are solved for each individual particle. This Lagrangian particle tracking module needs to be incorporated into the existing SPARKLE scheme/layout which is defined above with reference to the Eulerian framework. This will be achieved using the following routines (Nair 2021):

- A particle interpolation routine will be applied to interpolate (Eulerian) instantaneous flow velocities found at the cell face centres (\mathbf{u}_i) (shown in Figure 3) to the nearby instantaneous particle locations ($\mathbf{u}(\mathbf{X}, t)$).
- A time integration routine will be used to advance particle positions and velocities with time.
- A particle communication routine will identify and transfer particles at processor boundaries to the relevant neighbouring processors.

The particle communication routine is particularly important, given that the SPARKLE direct numerical simulation process naturally involves 'domain decomposition', a process in which the domain is allocated equally amongst multiple processors of a high-processing computer. For example, the simulations in this report will contain 384 cells in the y-direction and 384 cells in the z-directions. In both directions, these cells will be divided amongst 12 processors, equating to a total of 32 cells per processor (as every core must be assigned the same number of cells to ensure simulations run without errors). Therefore, if a particle moves between cell number $(32\mathbf{n})$ and $(32\mathbf{n} + 1)$ in the y or z-direction (where $\mathbf{n} \in \mathbb{Z}^+$), it will be transferred between cores, and the particle communication routine will act to ensure this particle is appropriately registered.

3.2 Initial Conditions and Parameters

The initial conditions and parameters have very important effects on the simulations, and their alteration will allow for accurate representation of a real-world human cough scenario. A simple 2D diagram of the simulated domain is shown below, in which some of the key parameters are labelled. The labelled parameters, along with other key initial conditions, are discussed below the diagram with reference to the 'base case' scenario.

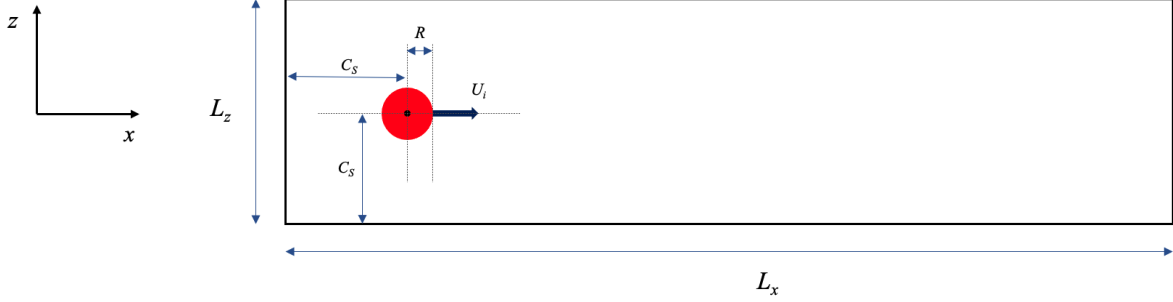


Figure 4: Diagram showing the domain associated with this report's model, labelled with some key parameters (Not to Scale).

- Domain Size:** The domain size is selected as $L_x = 3\text{m}$, $L_y = 0.5\text{m}$ and $L_z = 0.5\text{m}$. These dimensions have been tuned to allow for the visualisation of the entire cough pattern, whilst minimising computational expense. They have also been selected to ensure the domain has an appropriate 'resolution' (given the number of cells in each dimension).
- Number of Cells:** This parameter essentially controls the 'resolution' of the problem. The domain size above is divided between the number of cells in each direction - $N_x = 1536$, $N_y = 384$ and $N_z = 384$. This gives an overall grid size of $1536 \times 384 \times 384$. It is vital that the length scales produced by this resolution are smaller than the smallest physical length scales that need to be resolved during simulation - this will become particularly important during turbulence when the scales reduce (down to the Kolmogorov scale). The resolution must be controlled to prevent the cell Re number from becoming too big and causing 'wiggles'. The cell Re is given by $U \delta x / \nu$, where $\delta x = L_x / N_x$. The number of cells in each direction also has to be a multiple of the corresponding number of processors, to ensure that these cells can be divided equally between the available cores.
- Initial Velocity Field:** The flow field associated with a cough is generated by an initial velocity component, which is assigned to a small volume of air that can ultimately be projected with an initial velocity dictated by the simulation parameters. An initial spherical domain will be used, to represent a small volume of air contained within a human mouth, and this will be defined using a point within the domain (with x, y, z co-ordinates of $C_s, L_y/2, C_s$) and a radius (R). To define the sphere of initial flow, the velocity values will be set as zero everywhere and then, any cells within a given radius of the central point will be assigned a non-zero velocity value corresponding to the initial parameters. A Gaussian distribution is applied to the velocity profile, which is centred about C_s , with minimum values at the edge of the sphere. This creates a smoother transition between the different velocity conditions,

reducing the large velocity gradients that may cause 'wiggles'. The Gaussian velocity profile is given as $U = U_i \exp(-r^2/2R^2)$, where $r < R$ and r is the distance from the centre of the sphere in any direction.

- **Initial Particle Seeding:** The particles are also seeded within the initial spherical volume, which represents an accumulation of sputum in a carrier's mouth. Seeding the particles throughout this spherical domain ensures that they are all subject to the same initial velocity as the air flow. Like the initial velocity field, the sphere is centred at $C_s, L_y/2, C_s$ and has a radius R .
- **Boundary Conditions:** 'Periodic' boundary conditions (BCs) will be applied to this problem on the left and right hand side of the domain. This means that particles leaving the domain on one boundary will re-enter the domain at the opposite boundary location. These BCs are not realistic, but are used to prevent particles from interacting with (or bouncing into) walls. It essentially allows for the simulation of an 'unbounded' domain. Periodic BCs will not be applied at the upper and lower domain boundary, which will be modelled using a 'free slip' BC ($du/dz = 0$, $dv/dz = 0$ and $w = 0$). This is used so that when particles settle, they simply leave the domain and do not reenter.
- **Initial Velocity:** This parameter (U_i) determines the initial velocity given to the spherical 'cough' domain in the x-direction. The selected magnitude of 10m/s is justified in section 2.5.
- **Particle Number, Spread and Size:** As mentioned in section 2, the aim of this project is to simulate a large range of particle sizes, and these will be distributed using a uniform distribution. The minimum radius will be set as $0.5 \mu\text{m}$, whilst the maximum radius will be set at $50 \mu\text{m}$. 25 equally distributed categories of particle size will be created within this range, and the total number of particles (50,000) will be distributed equally between them (2,000 particles within each size range). These numbers have been tuned to allow a large spread of particles and a satisfactory number within different size categories, whilst also ensuring that the total particle volume approximately matches the characteristic volume of saliva emitted in a cough (6.62 mm^3) (VanSciver et al. 2011).
- **Initial Sphere Location and Radius:** These parameters have been controlled to ensure the point of release is in the middle of the y and z-domain, and also far to the left of the x-domain (to allow the dispersion pattern to evolve in the positive x-direction). The radius has also been selected to try and match the volume of air projected by a human cough. Based on this, $C_s = 0.25\text{m}$ and $R = 0.025\text{m}$.
- **Viscosity:** The viscosity (kinematic) ν is also used as a means of controlling the cell Re number ($Re = U\delta x/\nu$) to prevent 'wiggles' from occurring. For the report's simulations, ν will be $1\text{e-}4$. This may seem large, but can be used to reduce computational expense without dramatically affecting the simulation (particularly for the turbulent case). As long as there are enough scales present, the simulation will conduct roughly the same process regardless of the viscosity, because the large scales contain most of the energy. Therefore, in principle, the fluid can be made more viscous to reduce the computational expense which is brought about by an increase in Re during turbulent simulations.

- **Simulation Time-Step:** The simulation time-step was iterated to prevent the time integration from becoming unstable. When the velocity components of the simulation increased, the time step was reduced to maintain stability. In the end the simulation time step was $1\text{e-}3\text{s}$ for the 'base case' and $5\text{e-}4\text{s}$ for the turbulent case.
- **Particle Density:** We will take the density of the particles (ρ_p) to be the standard density of human sputum (1.012 g/ml) (Kubala et al. 2018). By doing this we assume that all particles are of the 'droplet' composition, and none of them are considered 'droplet nuclei' which will have a different density. This is an acceptable assumption, as the timescale required for the evaporation of droplets to induce substantial changes in composition (and thus density) will be larger than the time scale for these simulations (Stadnytskyi et al. 2020).

Other parameters such as 'simulation run time' and 'data sampling time interval' are readily understood and are thus not included above. The run time was generally controlled by the simulation wall-time, which was set at 16 hours, giving simulation data between 6s and 12s (depending on whether turbulence was incorporated).

3.3 Incorporating Grid Turbulence

As well as the 'base case' scenario, in which a cough is projected into a quiescent background, analysis will also be conducted for a scenario in which the same model cough is projected into a turbulent background. To achieve this, the initial parameters and conditions from the 'base case scenario' will be applied, but an additional initial condition of 'background turbulence' will be imposed. DNS will be used to run a simulation for homogeneous isotropic grid turbulence, which will output field files for the initial flow. These field files will then be applied as the initial condition for the turbulent scenario, which will allow the turbulent flow structures to evolve in both space and time, interacting with the particles accordingly (Nair 2021).

The turbulent case setup used in this report is designed to closely resemble the turbulent flow in wind tunnel experiments (as is typical of grid-turbulence simulations) and is explained in greater detail in chapter 6.2 of Nair (2021). A passive grid will be used, and the DNS code will simulate the turbulent flow induced just downstream of this structure. An initial velocity distribution will be created, which contains contrasting velocity components at the grid and elsewhere in the domain (the exact distribution used can be seen in Nair (2021)). Once this has been done, the flow will be perturbed with random noise and will be allowed to transition into isotropic, homogeneous turbulence, which will form the basis of the turbulent initial condition (Nair 2021).

4 Results, Interpretation and Discussion

4.1 Quiescent Background - Base Case Scenario

After extensive tuning, the SPARKLE code was able to produce detailed results that allow for the subsequent analysis of the effects of particle sizes in the 2 different scenarios. The 'base case' scenario will be analysed first, before the effects of grid turbulence are incorporated.

4.1.1 The Flow Field

Although the primary aim of this project is to analyse the impacts of size on particle dispersion, analysis of the flow will be vital in understanding the physics of particle dispersion. An example of this is highlighted below.

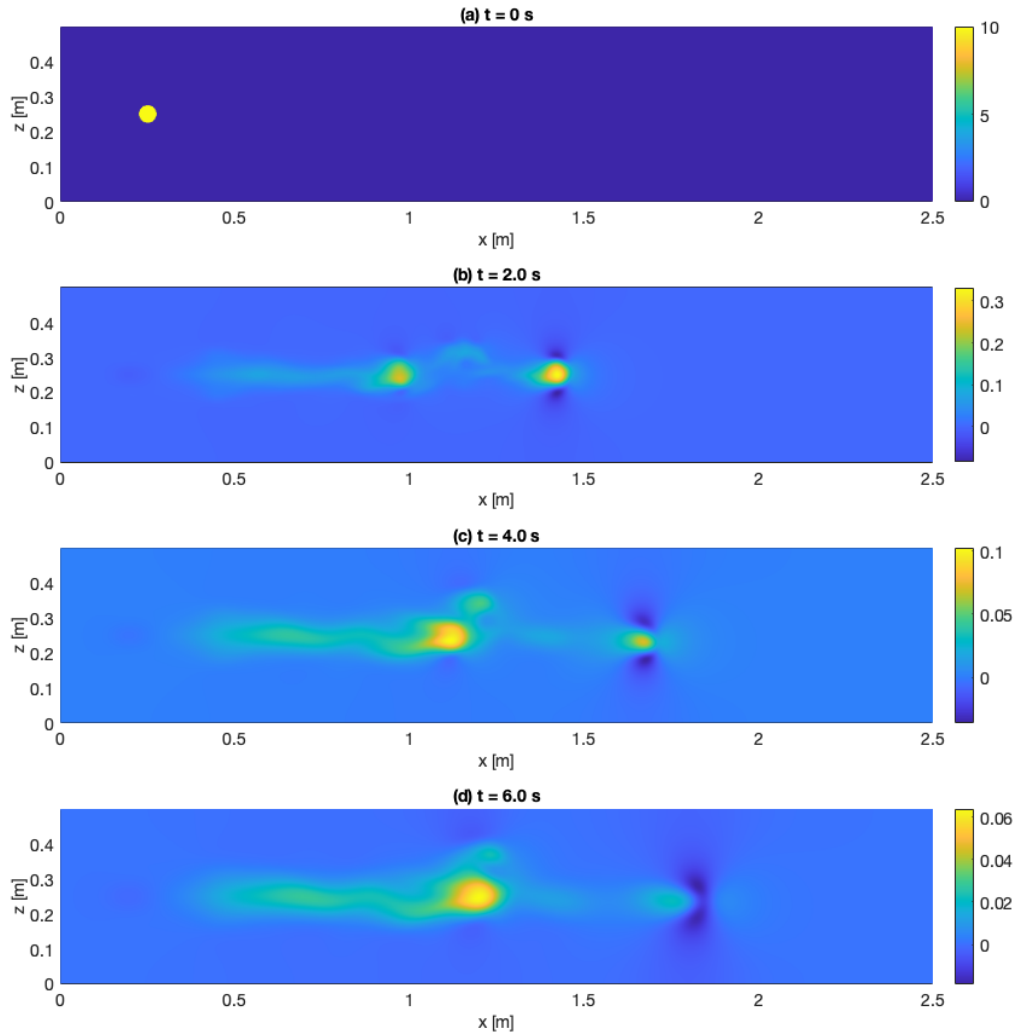


Figure 5: Freeze-frame Horizontal Velocity fields (u) [m/s] depicted at different time-steps - (a) $t = 0$ s, (b) $t = 2$ s, (c) $t = 4$ s, (d) $t = 6$ s

The flow pattern is shown above in *Figure 5*, which contains freeze frame images depicting the initial horizontal velocity field (u) at 2 second time intervals, for the first 6 seconds after release. The pattern seen here shows the development of a jet, which is characterised by the presence of two *pulse* vortex rings, that propagate through the domain. This pattern is expected and is typical of a spherical/circular accumulation of fluid that is impulsively given a certain momentum (Akhmetov 2009). A vortex ring is a toroidal volume of vortical fluid that moves in a surrounding medium at a translational speed perpendicular to the ring plane (Akhmetov 2009). In this scenario, the spherical accumulation of compact fast-moving fluid will emerge from its initial domain, but as it is projected into the quiescent environment, an interface will be created at the front of the sphere between the fast-moving and stationary fluid, at which a heightened level of viscous friction will develop. The friction induced at this front boundary, as the vortex ring moves through the quiescent fluid domain, will reduce the velocity at the front edges of the ring. As the fluid at the front of the sphere decelerates, the faster fluid behind the front interface coming through the centre of the ring will displace it, creating a circulation pattern, as the slower fluid that is displaced slips around the mass, curling back to form a 'mushroom cloud'. Additionally, as the slow fluid reaches the back of the sphere, it is drawn into the faster moving fluid in the centre of the ring. This axisymmetric circulation revolves about the ringed axis commonly referred to as the 'torus' (Akhmetov 2009). The circulation of flow about the 'torus' in the vortex ring is more visible in moving graphics that include the smallest aerosol particles simulated. These particles act as passive tracers and allow for a clear visualisation of the circulatory movement within the vortex atmosphere. However, in *Figure 5* (b), (c) and (d), the presence of a vortex ring can be confirmed by the negative velocities found on the top and bottom edges of the sphere. This shows that the velocity is in the positive x-direction through the centre of the sphere, but in the negative x-direction on its upper and lower boundaries - confirming the presence of circulation (about a torus).

It is also important to note that a secondary pulse ring seems to be formed in the wake of the first vortex ring. In fact, after 2.2 seconds, the velocity of the secondary ring exceeds that of the main vortex ring. This is shown in *Figure 6* which tracks the x-location of maximum velocity in the horizontal velocity field.

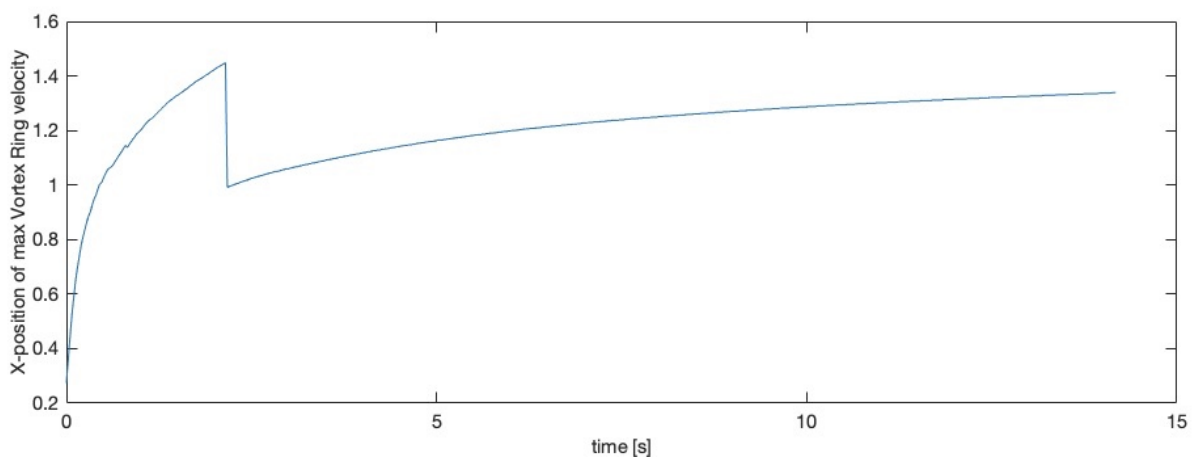


Figure 6: Figure showing the x-location [m] of the maximum horizontal velocity (in the velocity field) against time

This is also highlighted in the *Figure 7*, which plots the integral of specific kinetic energy (with respect to z) against both x and t (on a logarithmic scale). Given that the density of the fluid is constant, the specific kinetic energy (kinetic energy per unit mass - E) can be given as follows:

$$E = \frac{1}{2}(u^2 + v^2 + w^2) \quad (15)$$

Using the velocity field data for the u , v and w components allows for the calculation of the specific kinetic energy throughout the domain over the full range of time steps. This can then be integrated over the z -direction and plotted with respect to the x -direction and the time. This ultimately shows that there are two distinctive peaks of kinetic energy moving through the domain (in the x -direction) with time, and this corresponds to the primary and subsidiary vortex rings. This subsidiary vortex ring has likely been induced due to the initial Gaussian velocity profile within the sphere. Had the problem been initialised with a typical 'vortex ring solution', two separate pulses would not have been produced. However, in the case of this Gaussian distribution, not all the fluid in the initial spherical domain will be wrapped into the initial vortex ring, and as a result, a secondary pulse will be induced with the remaining fast-moving fluid from the initial domain.

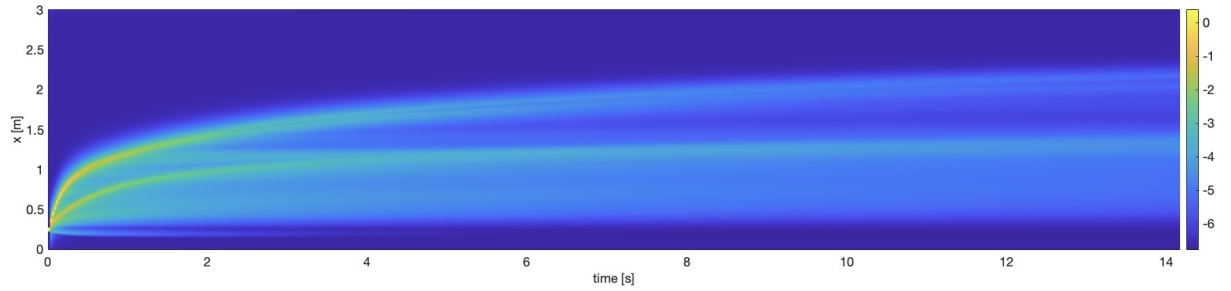


Figure 7: Figure showing the Specific Kinetic Energy (integrated over z) (E) [m^2/s^2] against x and t - plotted on a logarithmic scale (base 10).

Finally, the enstrophy can be plotted to help gauge the level of vorticity present within the flow field, which will be able to confirm the presence of a vortex ring. By conditioning the flow statistics on the enstrophy, the presence of rotational energy can be analysed throughout the domain. Dimensionally, enstrophy is to vorticity what kinetic energy is to velocity, and it is denoted by $\omega^2 \equiv \omega_i \omega_i$, where ω_i is a vorticity component at a given point in the field (Davidson et al. 2008). Plots of the enstrophy field (*Figure 8*), show a direct comparison between the irrotational fluid outside of the jet and the rotational fluid about the centre points of both the primary and subsidiary vortex ring.

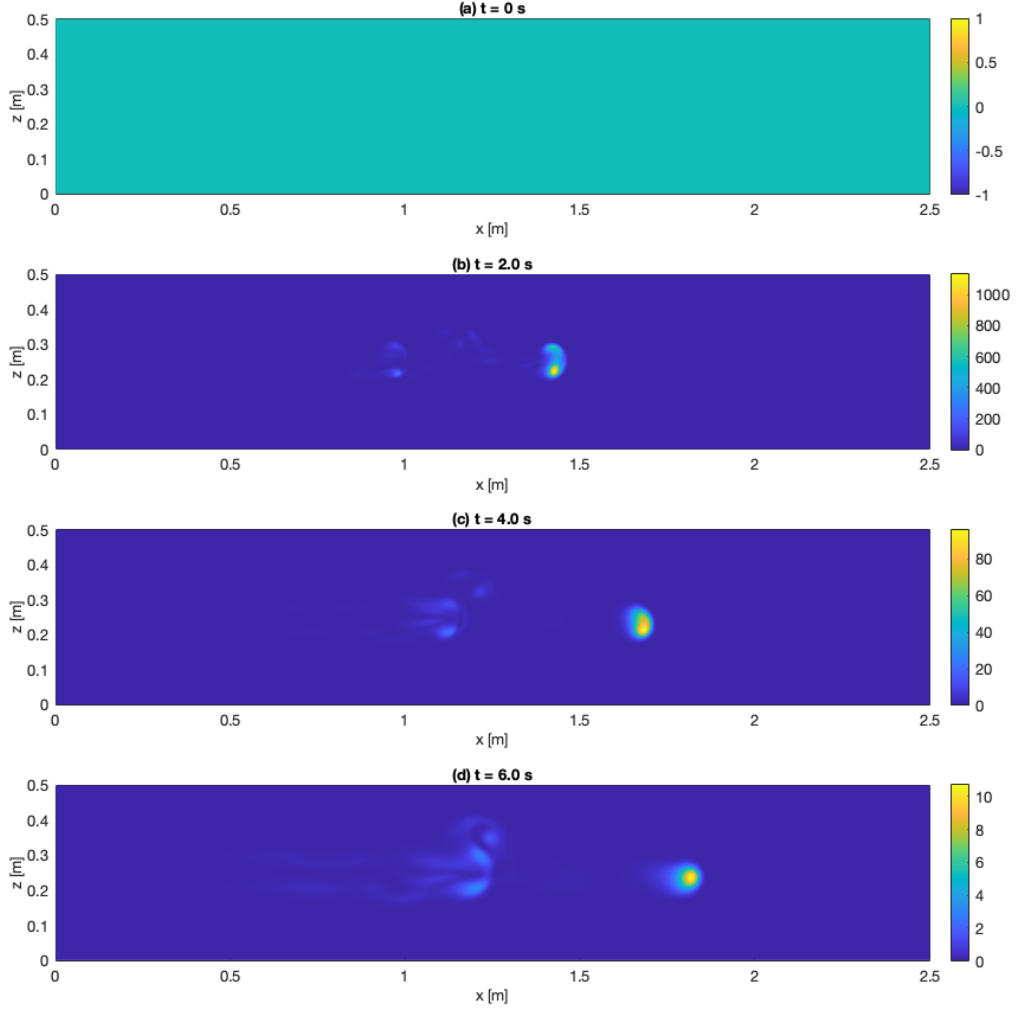


Figure 8: Freeze-frame Enstrophy fields (ω^2) [rad^2/s^2] depicted at different time-steps: (a) $t = 0\text{s}$, (b) $t = 2\text{s}$, (c) $t = 4\text{s}$, (d) $t = 6\text{s}$.

Notably, although the subsidiary ring exceeds the primary ring in both velocity and kinetic energy after $t = 2.2\text{ s}$, the enstrophy associated with the primary vortex ring is never exceeded anywhere else in the domain at any time-step. This is expected, because the highest vorticity will be found at the *initial* interface between the fast-moving and quiescent fluid, where viscous friction induces a strong rotational force (causing the fluid at the interface to curl back). The vorticity of this second pulse will not be as high as that of the first. This is due to the fact that, in the wake of the first ring, the discrepancy in fluid velocity on either side of the second ring's front boundary will not be as great, meaning that less viscous friction will be induced at this boundary (compared to that of the first ring), causing less rotation. Moreover, close examination of the enstrophy field in Figure 8 (b) shows that the heightened rotational energy in the second vortex could be enhanced by an Eddy induced downstream of the primary vortex ring. Although the secondary ring/pulse will have its own vorticity, it is quite likely that the first ring will leak vorticity, which will contribute to the rotational dynamics of the subsidiary ring.

Importantly, the analysis of enstrophy will become considerably more important when examining turbulent backgrounds. This is because the presence of background turbulence will induce localised vorticity throughout the domain.

4.1.2 Particle Behaviour

As previously mentioned, the particles were seeded throughout the initial spherical domain, and were projected with an initial 'coughing' velocity. As a result, the particles will be contained within the flow field and there will be significant feedback between the flow and particle behaviour. Sequential plots of the particle positions are shown in *Figure 9*, within which the particles are grouped based on size (using colour) into 5 equidistant categories, to fully articulate the effects of different particle sizes. Notably, the two separate toroidal clusters of particles within the primary pulse confirm the presence of circulation and thus the correct identification of a vortex ring structure.

The behaviour of these different particle sizes can predominantly be analysed through the particle Stokes number and the physics that underpins this concept, this is discussed in detail in section 2.2. Analysis of the upper and lower bound particle Reynolds numbers using equation (8), confirms that, after a short time increment, almost all of the particles present in the flow can be considered to be in the Stokes Regime (Lloyd 2003). The Stokes regime is classified when the particle Reynolds number is less than unity ($Re \ll 1$). Given that the smallest particle diameter is $1\text{ }\mu\text{m}$ and the largest is $100\text{ }\mu\text{m}$, after just 0.7 seconds of the base scenario, the upper bound particle Re number is 0.957, whilst the lower bound value is 0.00957. Therefore, assuming the 'base case' scenario is predominantly within the Stokes regime is an acceptable assumption. Within the Stokes regime, the application of Newton's II Law can be used to derive an analytical relationship for the particle response time (τ_p), which is given in equation (7). If we assume the flow scales are relatively constant throughout the domain in the quiescent case, the Stokes number for a given particle will mainly depend upon the particle response time (as the effect of τ_f will be minimal). Based on this, small particles with low values of τ_p will exhibit particle velocities that approach the surrounding flow velocity very quickly. Conversely, large particles with greater values of τ_p will take a very long time to approach the velocity of the fluid flow.

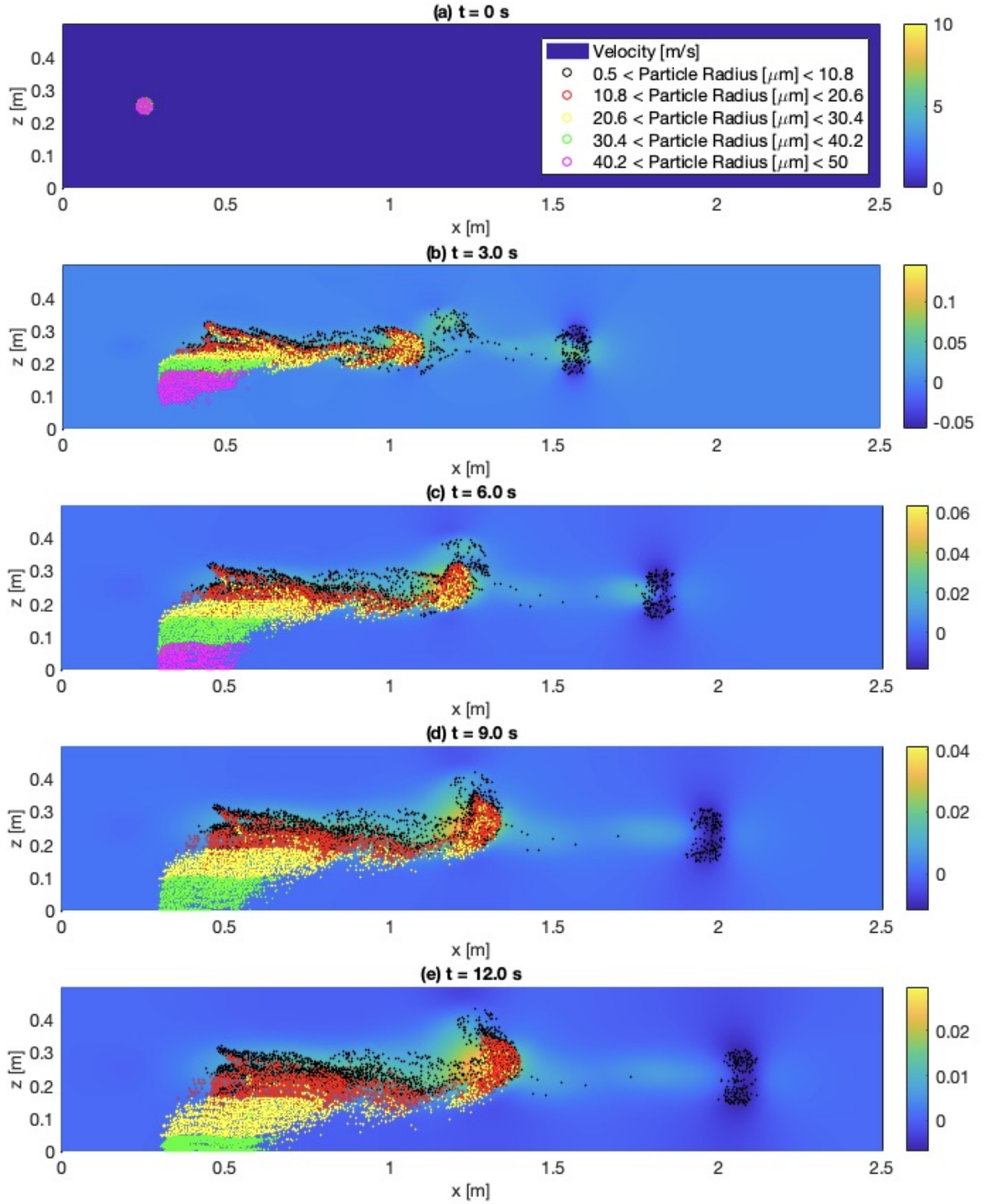


Figure 9: Figure showing the velocity field and the Particle positions (for different size categories) at $y=0.25$ for different time steps: (a) $t = 0$ s, (b) $t = 3$ s, (c) $t = 6$ s, (d) $t = 9$ s, (e) $t = 12$ s.

This is perfectly illustrated by *Figure 10*, which shows a lag time between the horizontal velocity of the vortex ring and that of different sized particles. Clearly, the particles with smaller radii/diameters will exhibit smaller particle response times and smaller Stokes numbers, and consequently, they will take less time to adopt the field velocity (in particular, that of the vortex ring). Therefore, for these smaller particle sizes, there will be a considerably smaller lag-time between the horizontal velocity of the vortex ring and the horizontal velocity of the particles.

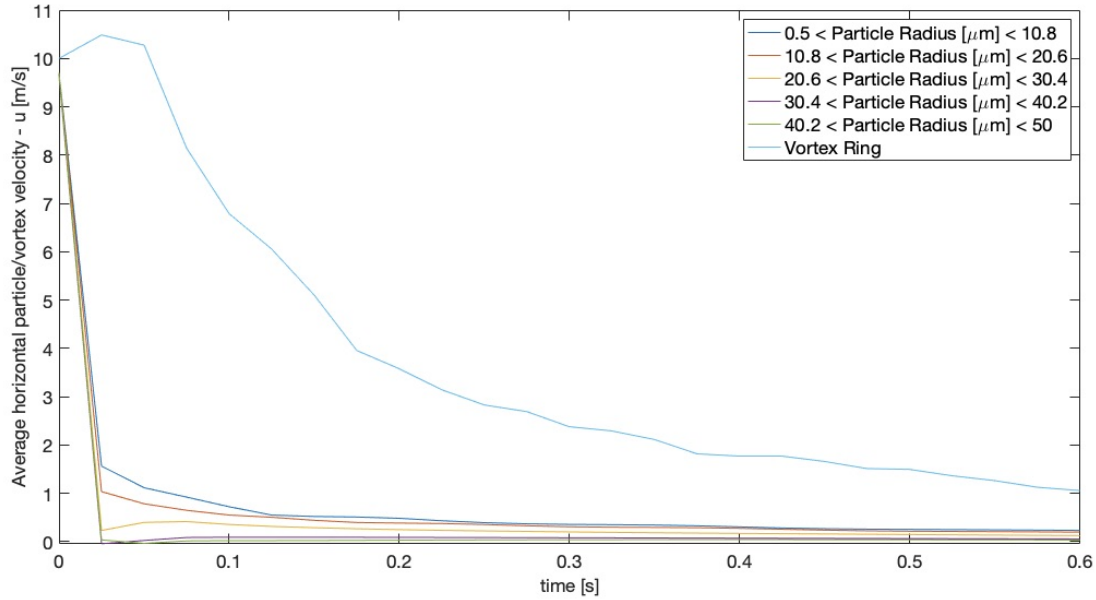


Figure 10: Figure showing the horizontal velocity (u) [m/s] of the vortex ring and the different particle size categories over time (for the first second after release).

The concept of particle response time can also be accurately illustrated with the settling velocities of different particle sizes. As discussed in section 2.6, the settling velocity of a spherical, non-rotating particle is directly proportional to the particle diameter squared, and is shown in equation (6). As the amplitude of the velocity within the flow field reduces over time, it is expected that the particles will tend towards an equilibrium state, which can be characterised by a steady settling velocity. As mentioned previously, the particle response time can be considered as the time required for particles to react to a new flow condition, or more simply put, a new 'force condition' (Liu 2020). Based on this, it is once again expected that larger particles will take more time to react to a change in the force condition, and will therefore approach a steady state settling velocity more slowly than smaller particles.

This concept is perfectly illustrated by *Figure 11*, which depicts the average experimental vertical velocity (w) of different particle sizes against time, along with the theoretical settling velocity (plotted in the same colour with a dashed line). The theoretical settling velocity was deduced by applying equation (6) to the entire particle population and then averaging within the depicted particle size ranges.

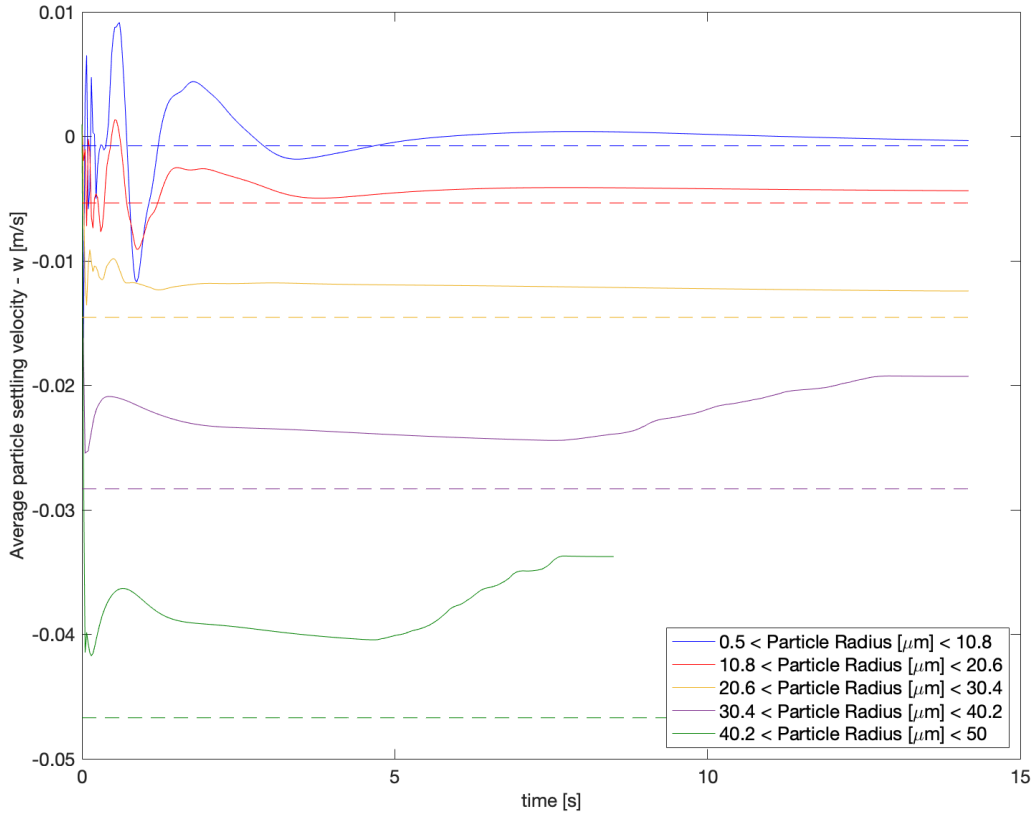


Figure 11: Figure showing the average vertical (settling) velocity (w) [m/s] against time with the theoretical settling velocity.

As is shown by the figure, the larger the particle size, the further away the experimental vertical velocity component is from the theoretical settling velocity and the longer it takes to reach it. The line graphs in *Figure 11* are characterised by two stages - firstly, there is a period of disturbance created by the initial coughing pattern, which may induce erratic transverse velocity components (particularly for smaller, lighter particles). This is sub-seeded by a calm state, at which the transverse (vertical) velocity will gradually tend towards the settling velocity. The 2 largest particle sizes exhibit a third stage (where the transverse velocity again deviates away from the settling velocity), but it is important to note that this increase (in the two largest size categories) arises due to the fact that these particles settle out of the domain at the bottom boundary. This is demonstrated in *Figure 12*, which shows the percentage of particles still present within each size category as a function of time. Notably, at $t = 4.65\text{s}$ the first particles within the range $40.2\mu\text{m} < \text{radius} < 50\mu\text{m}$ start to fall out of the domain and, at $t = 8.37\text{s}$, all particles in the range $40.2\mu\text{m} < \text{radius} < 50\mu\text{m}$ have settled out of the bottom boundary and the first particles in the range $30.4\mu\text{m} < \text{radius} < 40.2\mu\text{m}$ start to settle. This perfectly demonstrates the effects of gravitational sedimentation.

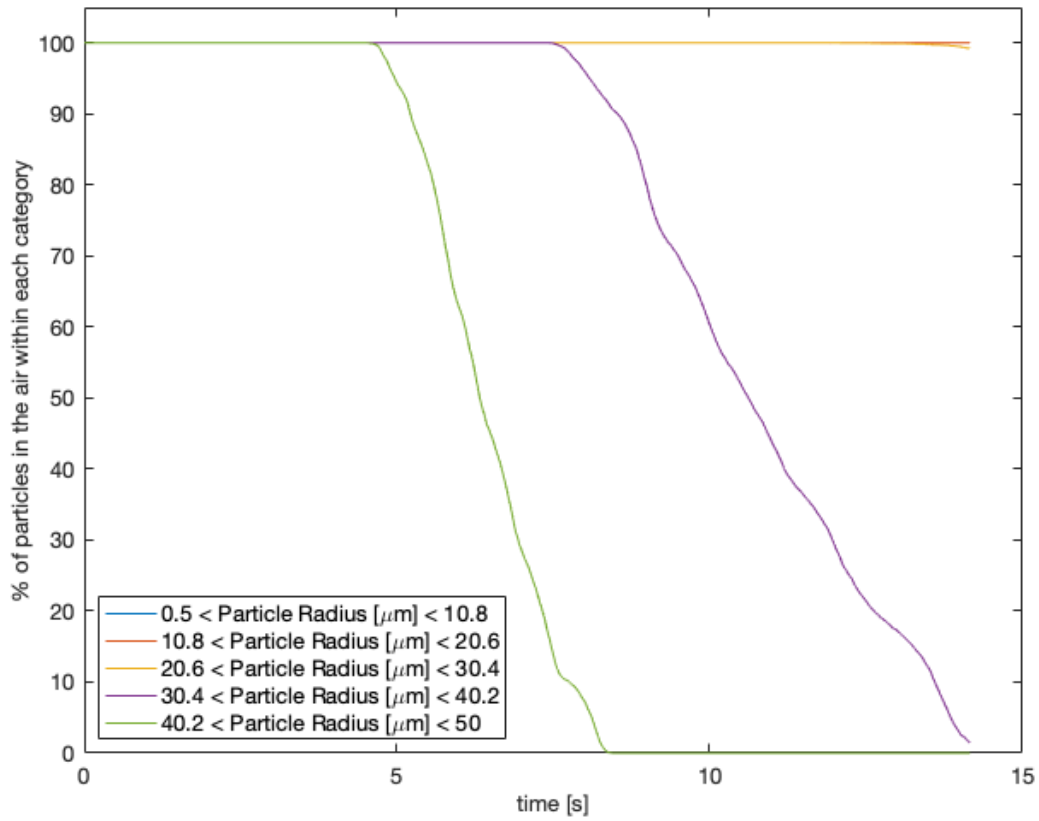


Figure 12: Percentage (%) of particles present within each size category against time.

Referring back to *Figure 11*, as the largest particles within each category settle out first, this leads to a temporary reduction in the settling velocity, just before all the particles have been removed. Had the bottom boundary been considerably lower down, the steady downward trend of vertical velocity would likely have continued (in a similar way to the smaller particle size categories), as the vertical velocity asymptotically tends towards the theoretical settling velocity value. As is expected, the particles in the smallest size category get closest to reaching the theoretical settling velocity because of their low particle response time, which means they take less time to adjust to the newly induced force equilibrium. However, in the smallest size category, after 14s the particles have still not reached the theoretical settling velocity, showing that the particles do not equilibrate as fast as expected. This proves that some of these small particles remain in the vortex ring (affected by the flow) and as a result, there will be a very long lag time before the particles reach the settling velocity associated with stationary fluid.

This data can also be used to determine which particle sizes are falling at a certain rate. For example, if a coughed particle (typically at head height) is to settle within 2 hours, it needs to settle at 0.75 m/hour (or alternatively $2.083\text{e-}4 \text{ m/s}$). By searching through the data at the final time step to see which particles have an absolute settling velocity less than this value, it can be deduced that **only** particles with a radius less than 3.1 μm (or similarly a diameter less than 6.2 μm) could feasibly be suspended in the air for more than 2 hours. This is expected, given the large lifespan of particles that are classified as aerosols (less than 5 μm in diameter).

The analysis in this section has primarily been conducted using the metric of particle response time (τ_p), which can be done as the fluid time scales in this quiescent scenario are relatively constant throughout the domain. This means that the Stokes number, which is $\gg 1$ for large particles and $\ll 1$ for small particles, will be almost entirely dictated by the particle response time which is in turn controlled by the particle size. This concept is confirmed by *Figure 12*, which depicts a highly idealised gravitational sedimentation scenario. Within this plot, at $t = 8.37s$, the first particles of size $30.4\mu m < \text{radius} < 40.2\mu m$ start to settle out of the domain, but not before all the particles in the size range $40.2\mu m < \text{radius} < 50\mu m$ have already settled. This shows that the particle behaviour, which is controlled by the Stokes number, is entirely dictated by the particle size. If there was a range of different flow scales, the Stokes numbers would vary for particles of the same size caught in different regions of the flow field. This would create considerable overlaps in *Figure 12*, as some particles of smaller sizes would leave the domain before larger ones. Therefore, although τ_f is not defined for the 'base case', it can be proved beyond reasonable doubt that the values of τ_f will not vary considerably and thus, the particle behaviour in the quiescent scenario is almost entirely dictated by the particle response time (which is controlled by the particle size).

Finally, the average centre of mass and spread (in both the x and y-directions) is plotted against time in *Figure 13*, to accurately display the effects of particle size on these key behavioural characteristics. The results depicted are as predicted, with smaller particles carried further in the x-direction and maintaining a more consistent elevation in the z-direction. It is important to note that the data in the two largest size categories will be subject to volatility, once the particles in these respective categories start settling out of the domain and the sample size for these statistics reduces. This is most clearly portrayed by *Figure 13 (d)*, which depicts the spread of particles in the z-direction. As particles in the larger size categories start to settle out of the domain, volatility starts to arise in the line graph, but more importantly, the spread statistic passes an inflexion point and starts to reduce as the particles remaining in the domain become clustered at the bottom boundary. Had the bottom boundary of the domain been larger, these statistics would probably show that, over time, the larger particles may in fact exhibit the greatest spread in the z-direction.

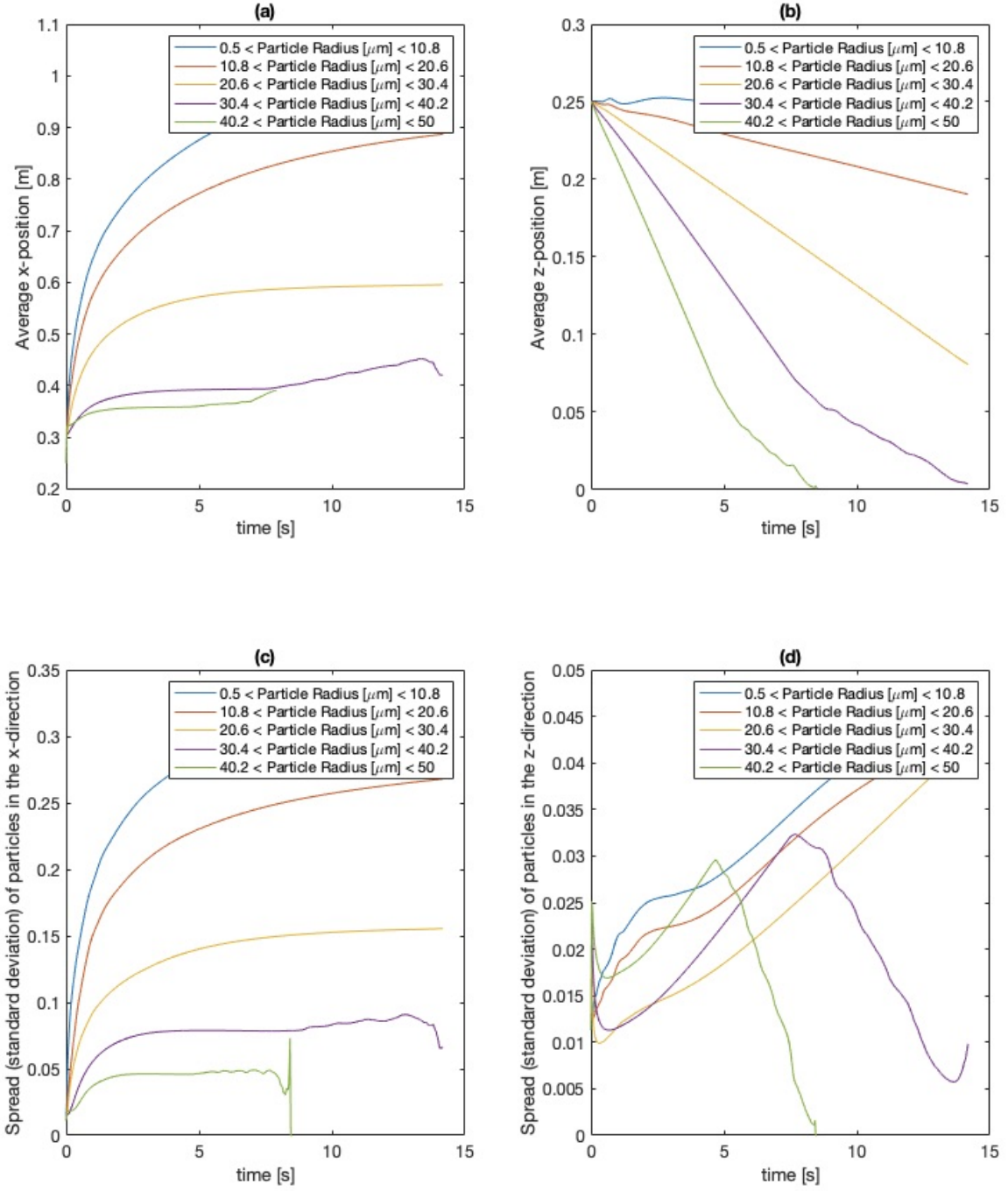


Figure 13: Plots showing (a) The average centre of mass in the x-direction against time, (b) The average centre of mass in the z-direction against time, (c) The spread of particles in the x-direction against time, (d) The spread of particles in the z-direction against time.

4.2 Background Turbulence Case

In the case of background turbulence, the time scales for the flow will vary throughout the domain between large Eddie scales and the smallest possible turbulent flow scale (the Kolmogorov scale). This means that, unlike the quiescent scenario, particles with the same radius *can* have different Stokes numbers, and will therefore be subject to very different particle dynamics. This turbulence is characterised by an initial volume averaged turbulent kinetic energy of $0.0102 \text{ m}^2 \text{ s}^{-2}$, which decays over time. As with the 'base case', the flow field will be analysed first.

4.2.1 The Turbulent Flow Field

Analysing freeze frames of the horizontal velocity (u) field at different time increments as shown in *Figure 14* will once again be important to the understanding of particle behaviour in this turbulent case.

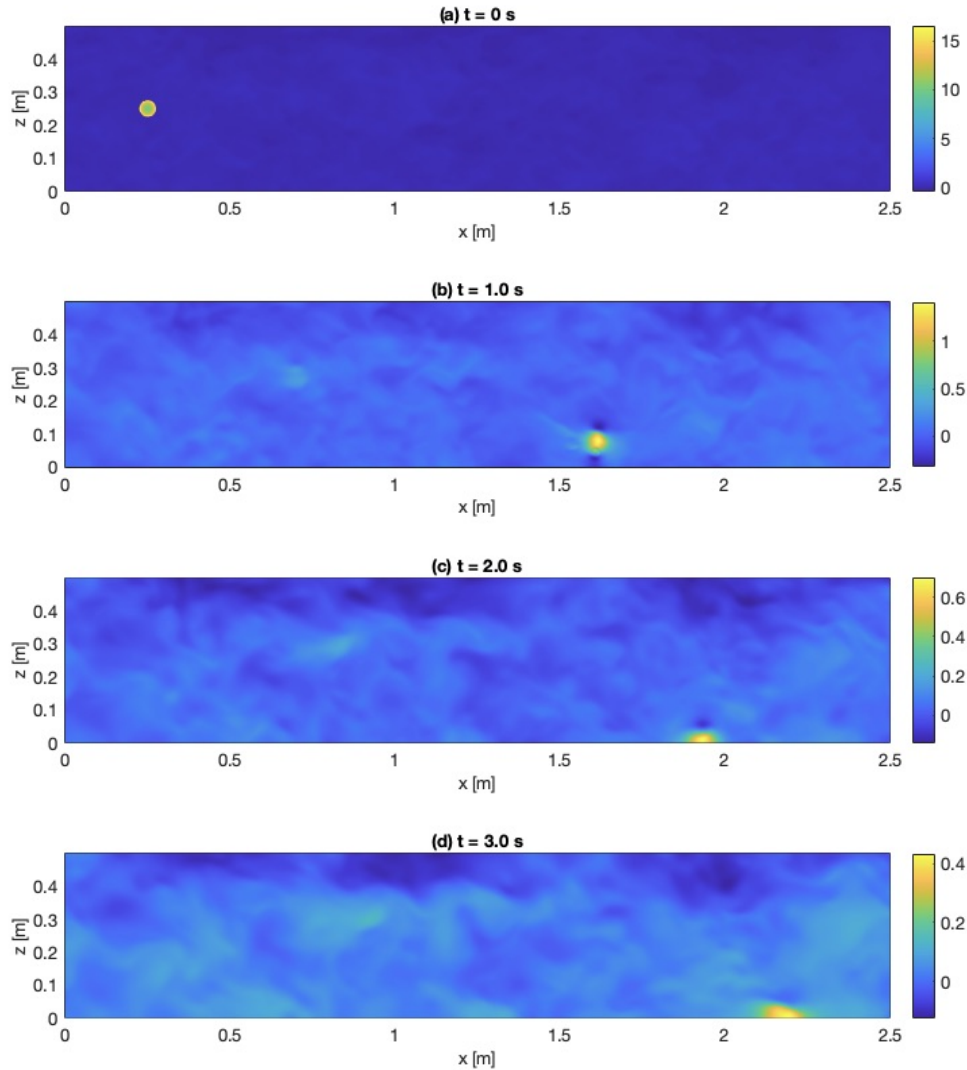


Figure 14: Freeze-frame of Horizontal Velocity (u) [m/s] fields for turbulent case depicted at different time-steps: (a) $t = 0 \text{ s}$, (b) $t = 1 \text{ s}$, (c) $t = 2 \text{ s}$, (d) $t = 3 \text{ s}$.

It is evident that the turbulent background will modify the behaviour of the two vortex rings seen in the 'base case' scenario. The first vortex ring still propagates through the domain, and clearly still possesses large rotational energy, which is evidenced by the presence of circulation (highlighted by the negative velocities on the top and bottom boundaries of the ring in *Figure 14* (b)). However, the path of the vortex ring is deflected, possibly due to the fact that the vorticity already present within the field as a result of the background turbulence deflects its path of travel, causing it to arc downwards. Importantly, the second vortex ring seems to have been muffled by the presence of the turbulent background. There is evidence of the second pulse at approximately $(x, z) = (0.7, 0.3)$ in (b) and (c), but its kinetic energy (and velocity) seems to have been dissipated by the background turbulence. In the 'base case' scenario, it was believed that the initial Gaussian velocity distribution meant that not all fluid from the initial spherical domain was wrapped into the first vortex ring and as a result, a secondary pocket of fast-moving fluid was produced. It is likely that this secondary pocket of fluid could have been disturbed by the turbulent background, before it could be wrapped into a subsidiary pulse ring. It is also worth noting that, over time, a boundary layer seems to develop at the top of the domain, between fluid moving in the positive and negative x -direction. This may have a notable effect on the behaviour of particles.

The most notable change to the flow field is the introduction of chaotic eddies, which are present throughout the domain and most clearly articulated by a plot of the enstrophy. Freeze-frames of the enstrophy field, plotted on a logarithmic scale at different times, highlight the presence of eddies throughout the domain (*Figure 15*). These localised pockets of vorticity, induced by this background turbulence, will have great effects on the behaviour of particles, as they will lead to considerable variation of the flow length scales in both time and space, directly impacting the particle Stokes numbers.

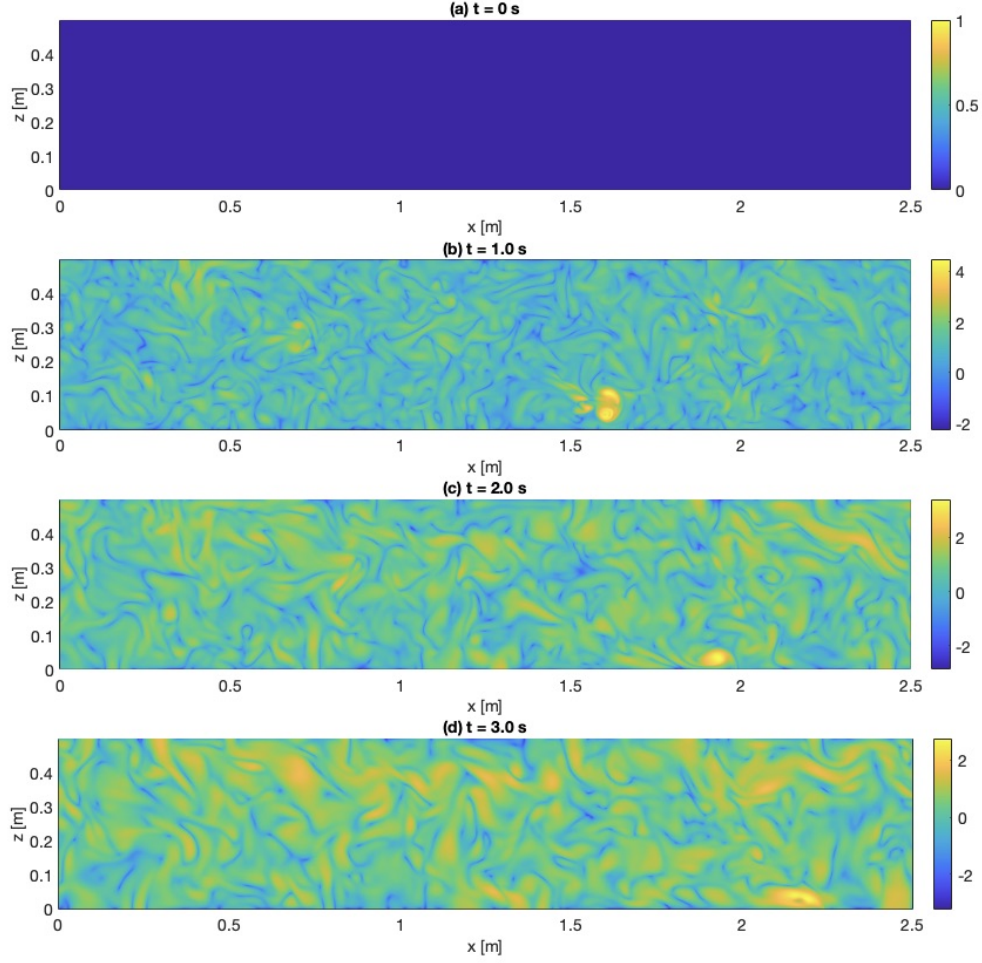


Figure 15: Freeze-frame of the Enstrophy (ω^2) [m^2s^{-2}] field plotted on a logarithmic scale at different time-steps: (a) $t = 0s$, (b) $t = 1s$, (c) $t = 2s$, (d) $t = 3s$.

Returning to the velocity field plots of *Figure 14*, by examining the magnitudes of the velocity components within this field at different time steps, a clear downward trend in velocity (and thus also kinetic energy) can be seen. This is expected, as the grid turbulence case introduced is characterised by a decaying level of turbulent kinetic energy, which is typically represented by an inverse relationship (AMS 2012). The statistics for these turbulent simulations were conditioned to monitor the turbulent kinetic energy (TKE) budget, and this allowed for a plot of the volume averaged TKE against time (*Figure 16*), which clearly shows that the decay depicted in *Figure 14* is present.

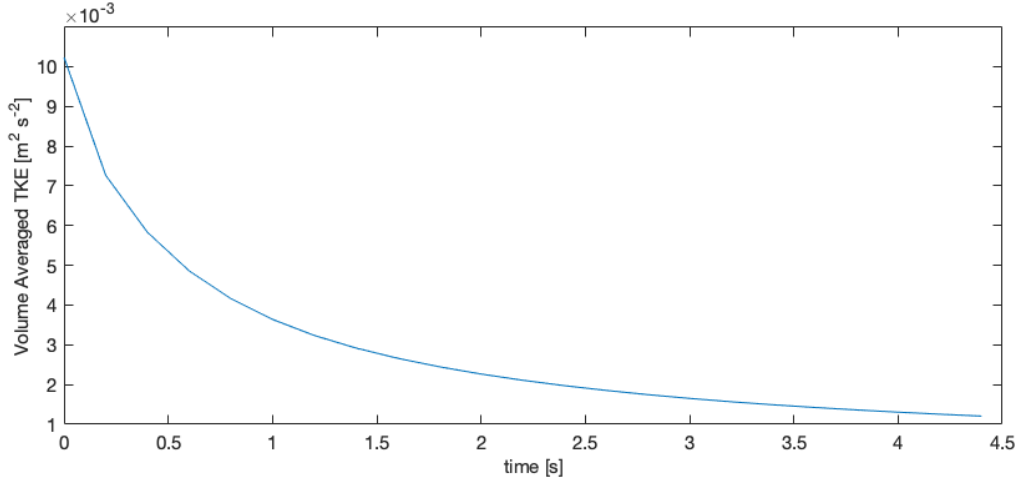


Figure 16: Plot showing the decay in the volume averaged Turbulent Kinetic Energy (TKE) [$\text{m}^2 \text{s}^{-2}$] over time.

As is typical of turbulence, energy will be injected into the system at large spatial scales, and following a cascading process, it will be dissipated at much smaller scales (MIT 2020). For a steady turbulent case, the dissipation rate at small scales must balance the energy injection at large scales. However in this research, the decaying grid turbulence case only involved an energy injection for a short initial time frame. Therefore, the energy input rate and dissipation rate were not balanced, leading to a steady decay in TKE. The average dissipation rate of TKE per unit mass (ϵ) was determined from the turbulent kinetic energy and is displayed in *Figure 17 (a)*.

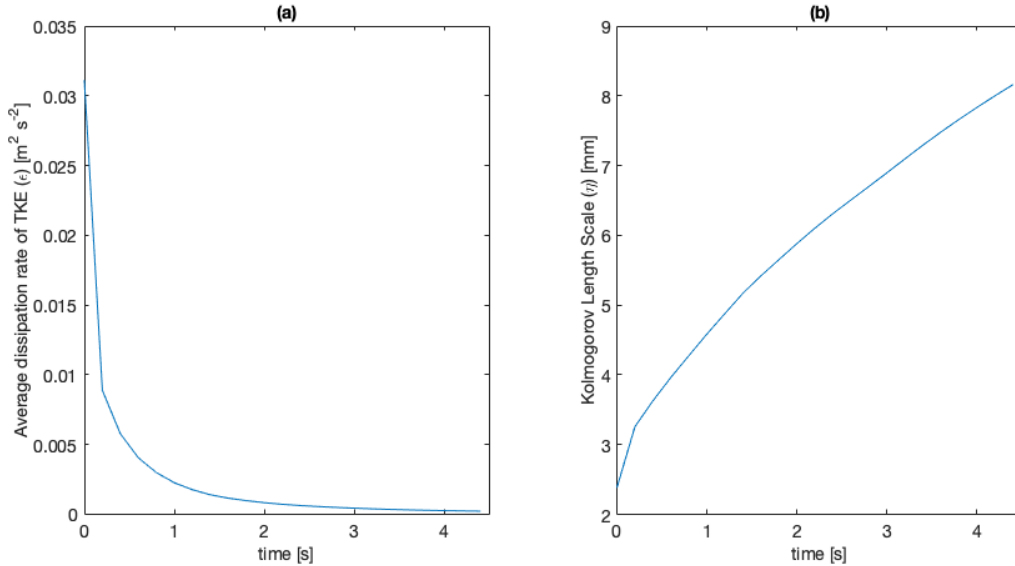


Figure 17: Plots showing: (a) The variation in the average TKE dissipation rate (ϵ) [$\text{m}^2 \text{s}^{-2}$] with time, (b) The variation in the Kolmogorov length scale (η) [mm] with time.

Given the inverse relationship between volume average TKE and time, the plot for dissipation rate (ϵ) against time will also follow a similar pattern, as the TKE decreases the most during the initial time-steps. Based on equation (10), the dissipation rate (ϵ) can be used to

calculate the Kolmogorov length scale (η), which is shown in *Figure 17* (b). Evidently, the decreasing dissipation rate induced by the decaying grid turbulence case will lead to an increasing Kolmogorov length scale. This will have large effects on the particles within the turbulent flow field, as this increase in the length scale will lead to an alteration of the Stokes number for particles, inducing a change in particle behaviour over time.

4.2.2 Particle Behaviour

It is believed that, within turbulent flows, inertial particles are centrifuged away from vortex cores or regions of high vorticity, generally accumulating in regions of low vorticity and high strain rate (Nair 2021). This is expected, as the local flow behaviour in these pockets of low vorticity will not be subject to regular change, and the flow scales will generally be larger than in the high vorticity eddies. Based on an analysis of Stokes law, it is therefore more likely that particles (that are unable to respond to changes at small flow scales) will accumulate here. *Figure 18*, which depicts the particle positions superimposed onto the horizontal velocity field at different time steps, shows that the particle cloud deforms irregularly to fit into the turbulent background. This evidently involves clusters of particles in regions of low vorticity, but also shows that the different length scales and velocity components cause particles of all sizes to travel in a range of directions. This ultimately induces considerably more mixing of particle sizes than in the quiescent scenario, where the majority of the particles settled in orderly layers governed by size. This is expected, and occurs because the varying flow (length) scales created by turbulence will cause particles of similar radii to have different Stokes numbers and thus disperse in a different way. Predictions are harder to make with this chaotic turbulent background, but the calculations suggest that particles with radii up to $8\mu\text{m}$ that have been carried upward by the turbulence could remain suspended in air for more than 2 hours. This contrasts the behaviour in the quiescent background, where only considerably smaller particles were expected to remain suspended in the air for this period of time.

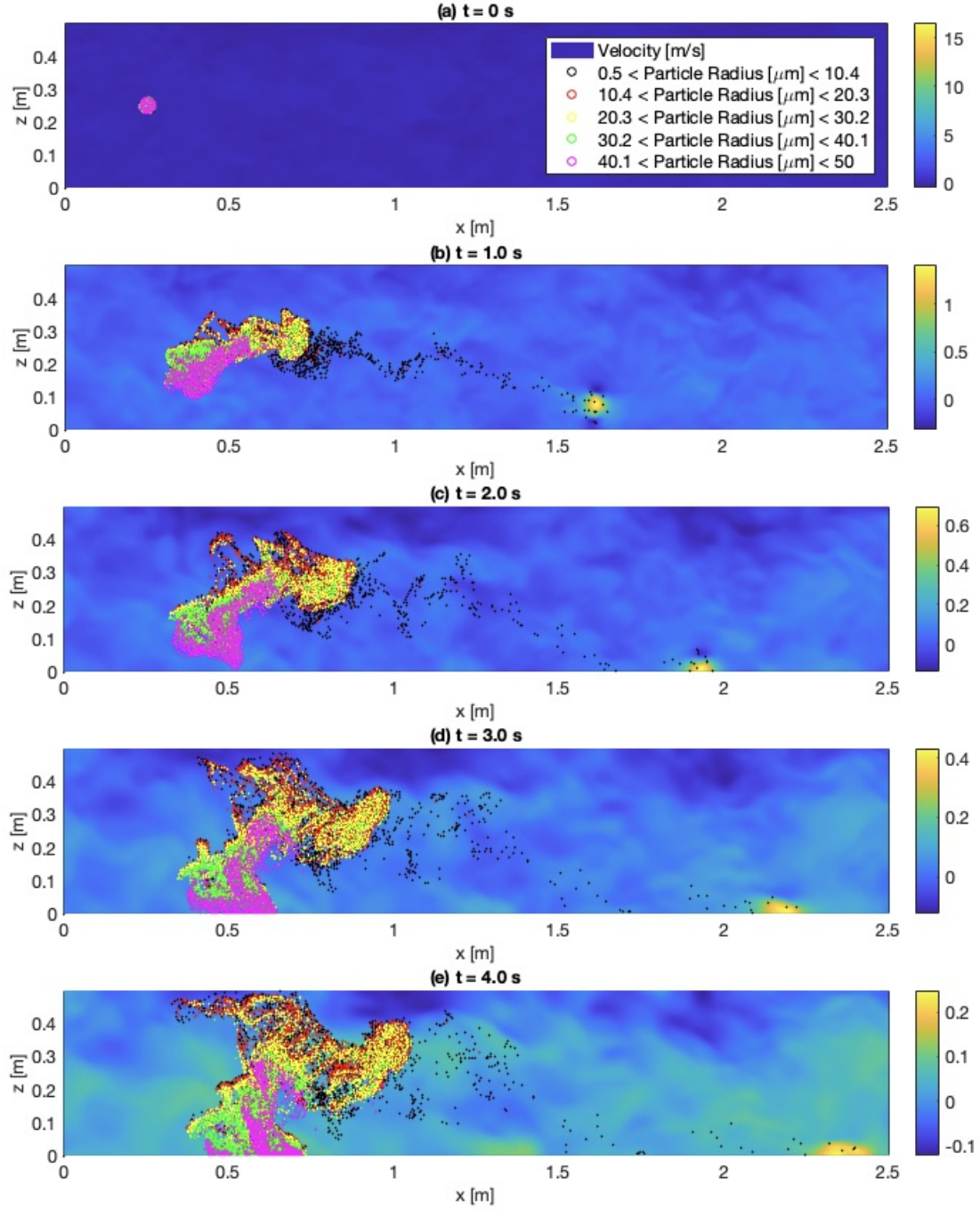


Figure 18: Figure showing the velocity field and the particle positions (for different size categories) at $y = 0.25$ for different time steps: (a) $t = 0 \text{ s}$, (b) $t = 1 \text{ s}$, (c) $t = 2 \text{ s}$, (d) $t = 3 \text{ s}$, (e) $t = 4 \text{ s}$.

To analyse the particle behaviour more effectively, some representative values of the particle Re , Stokes number (Stk) and dimensionless settling parameter (S_v) will be calculated for different particle sizes and at two different times. This will be done using average values for particle radius and settling velocity within the different size categories. The Reynolds number (Re) will be calculated using equation (8) and the average horizontal field velocity, the Stokes number (Stk) will be calculated using equation (9) with the Kolgomorov length scale (making it an upper bound value) and the non-dimensional settling coefficient (S_v) will be calculated using equation (12) and the average settling velocity.

Table 3: Characteristic values of Re , Stk and S_v at $t = 1s$ for different particle sizes.

Size Category	Re	Stk	S_v
$0.5 \mu m < \text{Radius} < 10.8 \mu m$	0.0022	1.808e-4	0.0303
$10.8 \mu m < \text{Radius} < 20.6 \mu m$	0.0071	0.0019	0.2345
$20.6 \mu m < \text{Radius} < 30.4 \mu m$	0.0120	0.0055	0.6538
$30.4 \mu m < \text{Radius} < 40.2 \mu m$	0.0170	0.0110	1.2885
$40.2 \mu m < \text{Radius} < 50 \mu m$	0.0219	0.0183	2.1384

Table 4: Characteristic values of Re , Stk and S_v at $t = 3s$ for different particle sizes.

Size Category	Re	Stk	S_v
$0.5 \mu m < \text{Radius} < 10.8 \mu m$	0.0019	1.2052e-4	0.0455
$10.8 \mu m < \text{Radius} < 20.6 \mu m$	0.0061	0.0013	0.3526
$20.6 \mu m < \text{Radius} < 30.4 \mu m$	0.0103	0.0037	0.9830
$30.4 \mu m < \text{Radius} < 40.2 \mu m$	0.0145	0.0073	1.9372
$40.2 \mu m < \text{Radius} < 50 \mu m$	0.0187	0.0122	3.2149

These results contain several notable details. Firstly, the Reynolds numbers for all size categories will generally be $\ll 1$. It is possible that in the case of really high velocities (such as those in the vortex ring) this may be violated, but ultimately we can assume that the vast majority of particles are in the Stokes regime, validating the method of calculating the Stokes number by using equation (7) for the particle response time (in the Stokes regime). The tables show that the Stokes number increases with radius (as expected), but it will also decrease with time. This is because the flow length scales will increase with time in line with a reduction of the average dissipation rate of TKE. Based on this, a given particle becomes more likely to respond to changes within the flow as the turbulent background evolves in time. On the other hand, the Kolmogorov velocity scale (μ_η) reduces over time, which means the non-dimensional settling parameter (S_v) will increase with time, leading to a reduction in clustering over time, as the effects of gravity become more dominant. This is observed in *Figure 18*, which shows

that particles are more likely to respond to changes in the flow over time, and also that particle clustering will generally decrease over time.

The following plots will compare certain statistics for the turbulent background case (which will be plotted with a solid line) with those for the quiescent background case (which will be plotted using a dashed line). These statistics can at times seem random, but that is due to the balancing of the effects of greater turbulence, with increased flow and rationality. In most cases, the turbulence will cause the Stokes number to increase, which in theory will make the particles more likely to fall out of the flow (and not respond). However, at the same time, the fact that there is more energy in the flow field, characterised by pockets of high velocity and vorticity, means that many particles that settled in an orderly fashion in the quiescent case will move in different and erratic ways. Additionally, particles of the same size will now have varying Stokes numbers due to the presence of turbulence, and this will induce erratic particle behaviour.

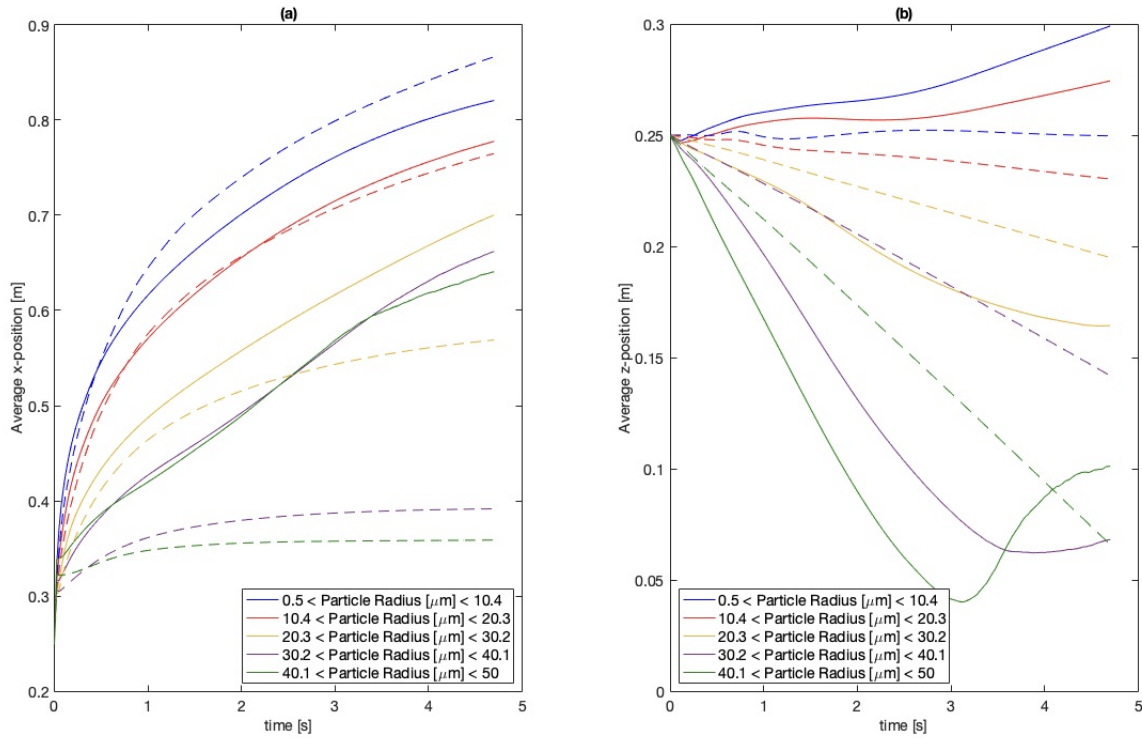


Figure 19: Figure showing the average centre of mass for particles in the: (a) x-direction (b) z-direction against time for both the turbulent (solid line) and quiescent (dashed line) case.

As can be shown in *Figure 19* (a), the presence of the turbulent background leads to an increase in the average distance of propagation in the x-direction for particles. The average centre of mass in the x-direction has notably increased for all cases apart from the smallest size category, with huge increases in propagation distance for the largest particles. It is believed that the result for the smallest size category is in fact an anomaly, induced by the fact that the vortex ring (which contains most of these small particles) is quickly deflected down and out of the domain, causing the spread to be under-predicted. By analysing moving graphics, it can be shown that the turbulent background will induce a localised vorticity near to the point of

release, which will cause the particles to curve round and travel in the positive x-direction as they are settling, leading to an increase in the distance of propagation.

The results in *Figure 19* (b) show that particles with a radius greater than $20.3 \mu\text{m}$ will fall to the ground faster, whilst lighter particles will actually move upwards. This phenomenon can be explained with the Stokes number. The smaller flow scales produced by background turbulence, will lead to larger Stokes numbers for particles, which are theoretically less likely to respond to changes in the flow. As a result, these larger particles will fall out of the flow and settle more quickly, as the average flow scale has reduced. These particles however, will not settle in orderly layers (like they do in the quiescent case) and this mixed layering is proof that the variety of time scales and flow patterns in a turbulent background will induce very different particle Stokes numbers (for particles of similar sizes) and therefore varied responses to the flow. The smaller particles (with smaller Stokes numbers) move upwards, as they have the ability to respond to changes in the flow and can thus be pulled upward by a rotating pocket of turbulent fluid.

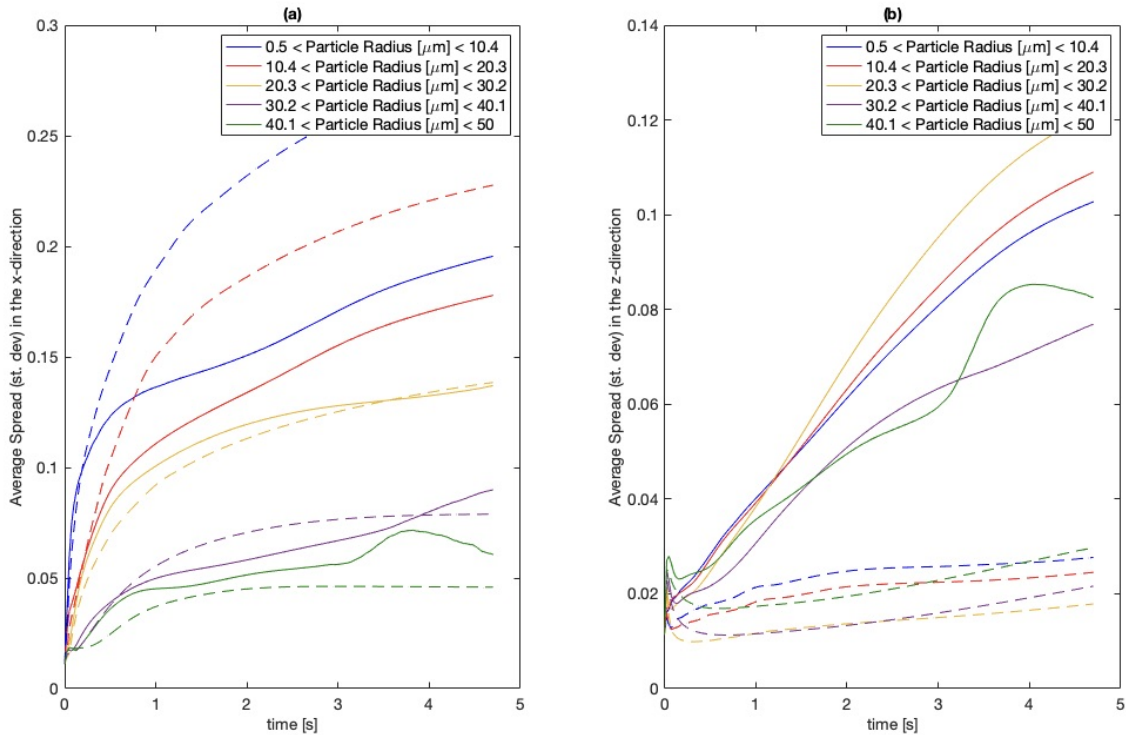


Figure 20: Figure showing the average spread for particles in the: (a) x-direction (b) z-direction against time for both the turbulent (solid line) and quiescent (dashed line) case.

As can be shown in *Figure 20* (a), although the results are very erratic, the presence of a turbulent background will actually lead to a reduction in the spread in the x-direction. This is because, in the quiescent case, the primary horizontal velocity component was the initial velocity of the spherical domain, whereas in the case of grid turbulence, opposing components of horizontal velocity are generated. The main reason why the spread of the small particle sizes decreases so dramatically, is that lots of these small particles are transported upwards (via rotational dynamics) to the top layer of the domain where the negative velocities are at their

greatest. This can be seen in *Figure 18* (d) and (e), where lots of these particles have been transported in the negative x-direction at the top of the domain.

On the other hand the results shown in *Figure 20* (b) for the spread in the y-direction are comprehensive, with all size categories showing a notable increase from the quiescent case. In this turbulent case, particle settling will still occur, particularly for particles with large Stokes numbers. However, the turbulent background will induce vertical velocity components that were not present in the quiescent case. This will occur on a range of fluid scales, which will allow for particles of many different sizes to respond, moving upwards and thus increasing the dramatically increasing the vertical spread.

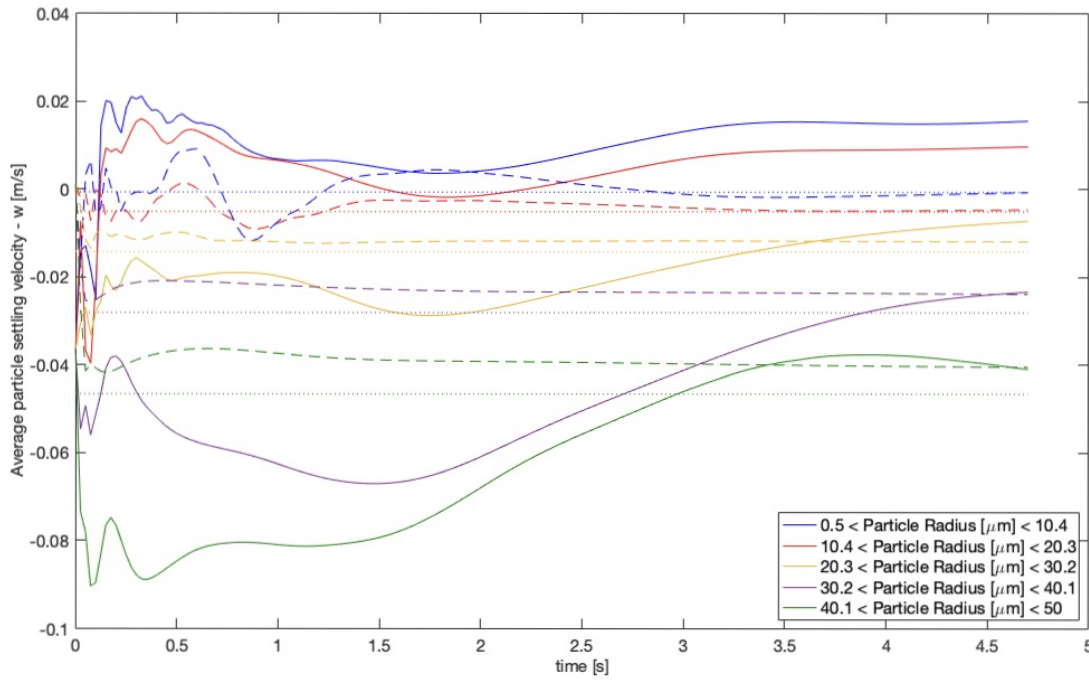


Figure 21: Figure showing the vertical velocity components (w) [m/s] against time for the turbulent (solid line) and quiescent (dashed line) case - the theoretical settling velocity (dotted line) is also included.

Finally, the vertical velocity components for the turbulent and quiescent case are plotted alongside the theoretical settling velocity represented by a faint dotted line in *Figure 21*. This highlights clearly that the disturbance induced by the background turbulence will increase the time taken for particles to equilibrate and approach their settling velocity. Based on an analysis of the Stokes number, it is expected that larger particles with a higher Stokes number will fall out of their respective flow field and equilibrate quicker. This is demonstrated by the comparisons between the velocities of the turbulent case and the theoretical settling velocities. From this, it is evident that larger particles approach their settling velocity more quickly. However, in the turbulent case, it is expected that the Stokes numbers will be larger than in the quiescent case and so, based purely upon an analysis of the Stokes number, the particles in the turbulent case should reach the theoretical settling velocity more quickly. However, the random nature of turbulence prevents this from happening, as particles of all sizes are affected by localised

vorticity and are drawn into clusters. This increased range of Stokes numbers for different particle sizes will ultimately lead to irregular particle movement, and as a result the particles will take more time to reach their terminal velocity, as the flow field dictates their behaviour.

5 Conclusions

Ultimately, this research project has shown how the characteristic of size affects the dispersion of COVID-19 particles in two background scenarios. In the quiescent background scenario, the particle behaviour could be almost exclusively analysed with the Stokes number and the particle response time, creating statistics which were predictable and logical to analyse.

However, in the turbulent case, the average reduction in the Stokes number for most particles was contrasted with the presence of increased energy and vorticity, as well as greater variation in flow scales in the background field. The random nature of the turbulence induced particle behaviour that was considerably harder to predict. In some cases the Stokes number was still useful for analysis, but in other cases, particularly when particles had been entrained in local pocket of vorticity, their behaviour became more unpredictable, particularly as the turbulence led to greater variation in the Stokes number itself. This research has shown that turbulence is not necessarily a risk factor in terms of the range of horizontal particle distribution, but through its localised vorticity it can induce vertical velocity components which bring medium sized particles to heights they would otherwise not reach. It is also possible that turbulent flows that move through a domain might enhance the lateral transmission of particles. It is very important to note that the presence of turbulence acts to centrifuge particles away from regions of high vorticity, creating regions of high particle concentration. This has important implications on virus transmissibility, as it creates regions where the probability of infection will be considerably higher (Stone 2021).

Ultimately, the main takeaway from this project is that, the introduction of turbulence will dramatically increase the range of flow scales, affecting the Stokes number and inducing considerably greater variation in particle behaviour than would otherwise be seen in a normal quiescent background scenario. The considerably more random and varied particle behaviour associated with background turbulence can act to violate the behavioural boundaries associated with droplets and aerosols. In the presence of turbulence, large droplets can be carried upwards and held in a pocket of low vorticity and high concentration. Additionally, particles with a radius of up to $8\text{ }\mu\text{m}$ (and a diameter of $16\text{ }\mu\text{m}$ - which is $9\text{ }\mu\text{m}$ larger than a characteristic aerosol), can be projected upwards at a velocity that will likely keep them airborne for over an hour. This analysis therefore shows that the means by which aerosols and droplets are arbitrarily contrasted in clinical science is extremely outdated. Instead of using arbitrary cut-offs based around size, lifespan or range to distinguish between aerosols and droplets, all respiratory droplets should be viewed as a continuous spectrum and the analysis of their behaviour should be based not just on their size but also on the background environment.

6 Evaluation and Future Developments

The research found in this report has effectively demonstrated the role of particle size in COVID-19 dispersion. The simulations conducted in this study have produced results that compare well against existing research and also show some of the existing oversights found in clinical science, with regards to the varying definitions of droplets and aerosols. Should this research be continued further, there are some minor drawbacks of this report's modelling that should be addressed.

Firstly, the simulations could be repeated in larger domains (closer to room size) and for longer times. Although this will come at a large computational cost, it may offer a better insight as to exactly what the different particle sizes do, from the moment of exhalation to settling. Although the research in this report has offered good insight into the particle behaviour, some statistics used to gauge the dispersion pattern (such as particle spread and average position) are constrained and negatively affected by the limits of the domain. As a result, a better comprehension of particle behaviour could be achieved by widening the boundaries. Once this has been done, simulations can also be run at greater turbulence intensities without diminishing the quality of data by having lots of particles transported out of the domain by turbulent flows.

Finally, the model could be extended to incorporate the evaporation kinetics of droplets, particularly if the simulations are going to be run at larger time-frames. It is generally believed that, over its entire lifespan in the air, a typical droplet will reduce to 20-40% of its original size due to the effects of evaporation (de Oliveira et al. 2021). This will have dramatic effects on the particle mass, which based upon the Stokes Number, will in turn induce huge variations in particle behaviour. At the time-scales simulated in this report, neglecting these effects was considered acceptable. However, for longer simulations, the evaporation kinetics will have to be incorporated into the SPARKLE code, such that the particle diameter changes with each time-step and the particle behaviour can be simulated at greater accuracy.

7 Acknowledgements

I would like to thank Dr Maarten van Reeuwijk for helping me with this project. He was an incredibly knowledgeable and engaging supervisor, who never missed a single meeting with me and was always willing to offer his help via an email or a Microsoft Teams calls. During these strange times in isolation, he was not only a great supervisor, but also a pleasure to talk to and share a joke with, even if it was through a screen. I am extremely grateful to have had him as my supervisor. I would also like to thank Vishnu Nair, who regularly took time away from his own work and his new-born child to meet me on Teams or send me long, technical emails about SPARKLE. His time and effort helped ensure that the simulations found in this report were as detailed as possible. Finally, I would like to thank the Imperial College Civil Engineering department as a whole for what has been a challenging but immensely enjoyable 4 years. I hope that our paths cross again in the future.

References

- Abuhegazy, M., Talaat, K., Anderoglu, O. & Poroseva, S. V. (2020), 'Numerical investigation of aerosol transport in a classroom with relevance to covid-19', *Physics of Fluids* **32**(10), 103311 1–13.
URL: <https://doi.org/10.1063/5.0029118>
- Akhmetov, D. G. (2009), *Theoretical Models of Vortex Rings*, Vortex Rings, Springer Berlin Heidelberg, Berlin, Heidelberg, pp. 5–32. ID: Akhmetov2009.
URL: https://doi.org/10.1007/978-3-642-05016-9_2
- AMS (2012), 'The glossary of meteorology'.
URL: https://glossary.ametsoc.org/wiki/Grid_turbulence
- Chao, C. Y. H., Wan, M. P., Morawska, L., Johnson, G. R., Ristovski, Z. D., Hargreaves, M., Mengersen, K., Corbett, S., Li, Y. & Xie, X. (2009), 'Characterization of expiration air jets and droplet size distributions immediately at the mouth opening', *Journal of Aerosol Science* **40**(2), 122–133.
- Craske, J. & van Reeuwijk, M. (2015), 'Energy dispersion in turbulent jets. part 1. direct simulation of steady and unsteady jets', *Journal of Fluid Mechanics* **763**, 500–537.
- Davidson, P. A., Morishita, K. & Kaneda, Y. (2008), 'On the generation and flux of enstrophy in isotropic turbulence', *null* **9**, N42. doi: 10.1080/14685240802491345.
URL: <https://doi.org/10.1080/14685240802491345>
- de Oliveira, P. M., Mesquita, L. C. C., Gkantonas, S., Giusti, A. & Mastorakos, E. (2021), 'Evolution of spray and aerosol from respiratory releases: theoretical estimates for insight on viral transmission', *Proceedings of the Royal Society A: Mathematical, Physical and Engineering Sciences* **477**(2245).
URL: <https://doi.org/10.1098/rspa.2020.0584>
- Debczak, M. (2020), 'Airborne vs. aerosol vs. droplet: What's the difference?'.
URL: <https://www.mentalfloss.com/article/622511/coronavirus-airborne-aerosol-droplets-whats-the-difference>
- Finlay, W. H. (2019), *Chapter 3 - Motion of a single aerosol particle in a fluid*, The Mechanics of Inhaled Pharmaceutical Aerosols (Second Edition), Academic Press, London, pp. 21–52. ID: 321338.
URL: <https://www.sciencedirect.com/science/article/pii/B9780081027493000038>
- Galbadage, T., Peterson, B. M. & Gunasekera, R. S. (2020), 'Does covid-19 spread through droplets alone?', *Frontiers in public health* **8**, 163.
- Han, Z. Y., Weng, W. G. & Huang, Q. Y. (2013), 'Characterizations of particle size distribution of the droplets exhaled by sneeze', *Journal of the Royal Society Interface* **10**(88), 20130560.

- Kubala, E., Strzelecka, P., Grzegocka, M., Lietz-Kijak, D., Gronwald, H., Skomro, P. & Kijak, E. (2018), 'A review of selected studies that determine the physical and chemical properties of saliva in the field of dental treatment', *BioMed research international* **2018**.
- Liu, Z. (2020), Biological and agricultural engineering - physical principles of environmental systems, Technical report, Kansas State University.
- Lloyd, P. J. (2003), *Particle Size Analysis*, Encyclopedia of Physical Science and Technology (Third Edition), Academic Press, New York, pp. 649–654. ID: 273169.
URL: <https://www.sciencedirect.com/science/article/pii/B0122274105005494>
- Maxey, M. R. & Riley, J. J. (1983), 'Equation of motion for a small rigid sphere in a nonuniform flow', *The Physics of Fluids* **26**(4), 883–889.
- MIT (2020), Isotropic homogeneous 3d turbulence, Technical report, MIT Open CourseWare.
URL: <https://ocw.mit.edu/courses/earth-atmospheric-and-planetary-sciences/12-820-turbulence-in-the-ocean-and-atmosphere-spring-2006/lecture-notes/ch6.pdf>
- Moriyama, M., Hungentobler, W. J. & Iwasaki, A. (2020), 'Seasonality of respiratory viral infections', *Annual Review of Virology* **7**(1), 83–101.
URL: <https://www.annualreviews.org/doi/10.1146/annurev-virology-012420-022445>
- Nair, V. S. K. (2021), Particle and droplet dynamics at cloud-environment interfaces, PhD thesis.
- Nicolaou, L. & Zaki, T. A. (2015), 'On the stokes number and characterization of aerosol deposition in the respiratory airways'.
URL: <https://core.ac.uk/download/pdf/77002685.pdf>
- Stadnytskyi, V., Bax, C. E., Bax, A. & Anfinrud, P. (2020), 'The airborne lifetime of small speech droplets and their potential importance in sars-cov-2 transmission', *Proceedings of the National Academy of Sciences* **117**(22), 11875–11877. pmid:32404416.
- Stone, H. A. (2021), "er hangt iets in de lucht" | één jaar coronapandemie | knaw video conference'.
- Tang, J. W., Bahnfleth, W. P., Bluysen, P. M., Buonanno, G., Jimenez, J. L., Kurnitski, J., Li, Y., Miller, S., Sekhar, C. & Morawska, L. (2021a), 'Dismantling myths on the airborne transmission of severe acute respiratory syndrome coronavirus (sars-cov-2)', *Journal of Hospital Infection* .
- Tang, J. W., Marr, L. C. & Milton, D. K. (2021b), 'Aerosols should not be defined by distance travelled', *Journal of Hospital Infection* **1**(1).
URL: [https://www.journalofhospitalinfection.com/article/S0195-6701\(21\)00210-3/fulltext](https://www.journalofhospitalinfection.com/article/S0195-6701(21)00210-3/fulltext)
- VanSciver, M., Miller, S. & Hertzberg, J. (2011), 'Particle image velocimetry of human cough', *Aerosol Science and Technology* **45**(3), 415–422.
- Verstappen, R. & Veldman, A. (2003), 'Symmetry-preserving discretization of turbulent flow', *Journal of Computational Physics* **187**(1), 343–368.

- Viola, I. M., Peterson, B., Pisetta, G., Pavar, G., Akhtar, H., Menoloascina, F., Mangano, E., Dunn, K. E., Gabl, R. & Nila, A. (2021), ‘Face coverings, aerosol dispersion and mitigation of virus transmission risk’, *IEEE Open Journal of Engineering in Medicine and Biology* **2**, 26–35.
- V’kovski, P., Kratzel, A., Steiner, S., Stalder, H. & Thiel, V. (2021), ‘Coronavirus biology and replication: implications for sars-cov-2’, *Nature Reviews Microbiology* **19**(3), 155–170.
- Wan, G.-H., Wu, C.-L., Chen, Y.-F., Huang, S.-H., Wang, Y.-L. & Chen, C.-W. (2014), ‘Particle size concentration distribution and influences on exhaled breath particles in mechanically ventilated patients’, *PloS one* **9**(1), e87088.
- WHO (2021), ‘World health organization coronavirus (covid-19) dashboard ’.
URL: <https://covid19.who.int/>
- Wurie, F., de Waroux, O. L. P., Brande, M., DeHaan, W., Holdgate, K., Mannan, R., Milton, D., Swerdlow, D. & Hayward, A. (2013), ‘Characteristics of exhaled particle production in healthy volunteers: possible implications for infectious disease transmission’, *F1000Research* **2**. pmid:24555026.
- Yang, S., Lee, G. W., Chen, C.-M., Wu, C.-C. & Yu, K.-P. (2007), ‘The size and concentration of droplets generated by coughing in human subjects’, *Journal of Aerosol Medicine* **20**(4), 484–494.
- Zhu, S., Kato, S. & Yang, J.-H. (2006), ‘Study on transport characteristics of saliva droplets produced by coughing in a calm indoor environment’, *Building and Environment* **41**(12), 1691–1702.
- Zuo, Y. Y., Uspal, W. E. & Wei, T. (2020), ‘Airborne transmission of covid-19: Aerosol dispersion, lung deposition, and virus-receptor interactions’, *ACS nano* **14**(12), 16502–16524.